5 Coal characterisation: advanced coal analyses

5.1 Introduction

Recent advances in coal analyses have led numerous researchers in establishing a more comprehensive model of the coal structure. Although conventional analytical techniques have formed the backbone of coal research for a number of decades, advanced strategies such as NMR, XRD, MALDI-TOF MS etc. have provided a novel method for estimating the molecular structure of coal. A combination of both conventional- and advanced techniques can lead to a more detailed understanding of the behaviour of coal during utilization and conversion. In this chapter the main aspects concerned with parent coal characterisation with the aid of advanced techniques are presented and discussed. The following relevant sections are addressed:

- Overview of advanced coal characterisation analyses;
- Advanced coal characterisation techniques and apparatus;
- Characterisation results and discussion.

As was done in Chapter 4, the advanced characterisation techniques and results will be discussed under different sub-sections within the text.

5.2 Overview of coal characterisation analyses

5.2.1 Advanced analyses

Advanced analyses refer to advanced analytical techniques such as ^{13}C NMR, MALDI-TOF MS, HRTEM, etc. that were used to assess the molecular characteristics of the

parent coals. A summary of the different advanced analyses conducted on the four coals is given in Table 5.1.

Table 5.1 Advanced characterisation analyses performed on the four coal samples.

Characteristic property	*Analysis*	*Laboratory responsible*
Molecular Structure	^{13}C NMR	University of Stellenbosch
	XRD carbon crystallite	XRD Analytical & Consulting
	HRTEM	University of Cape Town
	MALDI-TOF MS	Pennsylvania State University

5.3 Characterisation techniques and apparatus

5.3.1 Advanced analyses

5.3.1.1 Additional sample preparation

For the advanced analytical techniques, further sample preparation was conducted to adhere to the constraints of the different analyses. Coal samples (as discussed in Section 4.3) were milled and sieved to an ultra-fine size fraction of -75 µm.

Demineralisation of coal samples

Advanced analytical techniques, such as ^{13}C NMR and XRD (carbon crystallite analyses) require the samples to be analysed to be demineralised prior to analyses. An extensive acid-leach wash with hydrofluoric acid (HF) and hydrochloric acid (HCl) was performed on all four coal samples (-75 µm) in order to reduce the mineral content of each coal. This was done to ensure minimal mineral matter effect during analyses (both XRD and ^{13}C NMR). It has been shown that the use of HF and HCl as lixiviants does not significantly alter the molecular structure of coal (Strydom *et al.*, 2011; Van Niekerk *et al.*, 2008), although a very small increase in –COOH content can occur. In the case of ^{13}C NMR analyses, the presence of paramagnetic centres due to a high abundance of coal minerals may cause the invisibility of the carbon resonance signal (Solum *et al.*, 1989). A combination of HF (CAS no.: 7664-39-3) and HCl (CAS

no.: 7647-01-0), as supplied by Associated Chemical Enterprises, was used for the demineralisation process. A 5 M (mol.L^{-1}) diluted HCl concentration was prepared from the 32% concentrated stock solution. HF, with a 48% concentration, was used as received.

50 g of the -75 µm raw coal was added, in a 4 mL (acid):1 g (coal) ratio, to 200 mL of the 5 M HCl solution in a polytetrafluoroethylene (PTFE) beaker. The contents of the beakers were stirred continuously for 24 hours with a magnetic stirrer, while the beakers were covered with Perspex lids to avoid any spillage. After stirring for 24 hours, the coal samples were removed from the acid by vacuum filtration and the filter residues were washed with 600 mL of de-ionized water. Following this, the dried coal filter residues were scraped from the filter paper and the process was repeated (with the same ratio of acid), but using HF as the lixiviant (Okolo, 2010; Van der Merwe, 2010; Van Niekerk, 2008).

The 24 hour leaching period with HF was again followed by vacuum filtration and washing with de-ionized water before commencing the final step of the demineralisation process which consisted of leaching again with the 5 M HCl solution. Finally, the filter residues were vacuum filtered once more and washed with 600 mL of de-ionized water. The partially-dried filter residues were dried further in a vacuum oven at 80°C for 24 hours to remove as much moisture as possible (Okolo, 2010; Van der Merwe, 2010; Van Niekerk, 2008) and subsequently stored under N_2. Proximate analysis was conducted on the demineralised samples to assess the efficiency of demineralisation.

Samarium (II) iodide treatment

Demineralisation of coal might contribute to the formation of free radicals due to the removal of inorganic cations constituted in coal functional groups such as carboxylic acid functionalities. It has been observed by Muntean *et al*. (1988) that these free radicals can obscure the intensity of some of the ^{13}C nuclei during ^{13}C NMR analyses. In order to eradicate this problem the demineralised coal samples were treated with samarium (II) iodide (SmI_2) in tetrahydrofuran (THF) (concentration of ≈ 0.1 M in THF) to reduce the paramagnetism without reducing the diamagnetic organic coal compounds (Muntean & Stock, 1991). Approximately 3 g of each of the demineralised coal samples were continuously stirred for 12 hours in the 0.1 M SmI_2 solution under an inert atmosphere (N_2). A ratio of 8 mL of 0.1 M SmI_2 solution to 1 g of coal was used. After treatment the reaction was quenched with 30 mL of de-ionized water and the

THF was evaporated (Van Niekerk, 2008). The remaining solution was filtered through a vacuum filter and the formed filter residue was washed with 500 mL of diluted HCl (2 M) to remove the remaining lanthanide ions. This was followed by washing the coal filter residue with an additional 500 mL of de-ionized water. The partially-dried filter residues were dried in a vacuum oven at 80°C for 24 hours to remove as much moisture as possible. The samples were subsequently stored under N_2.

5.3.1.2 Solid-state ^{13}C nuclear magnetic resonance spectroscopy (^{13}C NMR)

After the SmI_2 pre-treatment, approximately 2 g of each of the demineralised coal samples were sent for ^{13}C NMR analyses to be conducted at the University of Stellenbosch. ^{13}C CP-MAS and DD experiments were performed on all four samples to investigate the structural differences, on a molecular level, between them (Assumption, 2010). Solid state NMR spectra were attained with the use of a Varian VNMRS 500 MHz, two channel spectrometer containing 4 mm zirconia rotors and a 4 mm Chemagnetics TM T3 HXY MAS probe. All CP-MAS experiments were conducted at ambient temperature with proton decoupling. Relaxation delays of 3 s were used, while 4000 scans were collected for adequate signal-to-noise. Radio frequency fields of $\gamma_C B_{1C} = \gamma_H B_{1H} \approx 55$ kHz were used to optimize the power parameters for the Hartmann-Hahn match. In addition, contact times of 2 ms were used for cross-polarization, while 3500 points Fourier transformed with a 50 Hz line broadening, were used for the free induction decay (FID) (Assumption, 2010).

Magic-angle-spinning (MAS) was performed at 12 kHz and hexamethylbenzene (HMB) was used as an external chemical shift standard (where the methyl peak was referenced at 17.8 ppm). Similar conditions were applied for the dephasing experiments. The interrupted decoupling time constant, t1Xidref, was, however, set to 40 µs after evaluating an array of time constants (Assumption, 2010). The obtained spectra were each phased- and baseline corrected manually before integration. The respective structural (aromatic- and aliphatic moieties) parameters were calculated from the integral values according to the method of Solum *et al*. (1989 & 2001). In addition, lattice parameters such χ_b and C can be estimated from the determined structural parameters with the aid of the following procedures. The mole fraction of bridgehead carbons (χ_b) can be calculated from Equation (5.1), as follows:

$$\chi_b = \frac{f_a^B}{f_{a'}}$$ Equation (5.1)

Furthermore, the average number of aromatic carbon atoms per cluster (*C*) is directly related to χ_b and can be estimated from the combined linear- and circular catenation model by:

$$\chi_b = 0.5\left\{\left[1-\tanh\left(\frac{C-C_0}{m}\right)\right]\chi_b^{'} + \left[1+\tanh\left(\frac{C-C_0}{m}\right)\right]\chi_b^{''}\right\}$$ Equation (5.2)

With $C_0 = 19.57$ and $m = 4.15$ directly obtained from Solum *et al*. (2001). The average number of attachments ($\sigma+1$) is another important lattice parameter describing the coal structure and is defined by Equation (5.3) as:

$$\sigma + 1 = \frac{\left(f_a^P + f_a^S\right)\times C}{f_{a'}}$$ Equation (5.3)

The fractional amount of all possible bridges intact (P_0) is described by the following equation as:

$$P_0 = \frac{f_a^P + f_a^S - f_{al}^*}{f_a^P + f_a^S}$$ Equation (5.4)

The determination of the last four lattice parameters: *B.L., S.C., MW* and M_δ are defined in Equations (5.5)-(5.8) (Solum *et al*., 2001):

$$B.L. = P_0(\sigma+1)$$ Equation (5.5)

$$S.C. = (\sigma+1) - B.L.$$ Equation (5.6)

$$MW = \frac{12.01\cdot C}{f_{a'}\times(\%Carbon/100)}$$ Equation (5.7)

$$M_{\delta} = \frac{MW - 13M_G C - 12 \cdot (1 - M_G) \cdot C}{(\sigma + 1)}$$ Equation (5.8)

5.3.1.3 X-ray diffraction (XRD)-carbon crystallite analyses

Apart from being a valuable technique for classifying the mineral fraction in coal, XRD has also been shown to be a useful tool in the study of the carbon crystallite properties of both coals and chars (Feng *et al*., 2003; Gupta, 2007; Lu *et al*., 2001; Maity & Mukherjee, 2006). XRD carbon crystallite analyses were performed on the demineralised coal samples using Co Kα radiation on the same apparatus as described in Section 4.5.1.1. Approximately 2 g of each of the demineralised coal samples were used for this purpose. An overview of the apparatus settings and analysis parameters used for the carbon crystallite analyses is provided in Table 5.2 (Okolo, 2010). During the course of the analyses the observed X-ray intensities were continuously measured and recorded by the X'Pert Highscore plus software. The obtained intensities (in arbitrary units) were processed further to enable the conversion to reduced intensity (Okolo, 2010). This was accomplished by first obtaining the raw diffractogram of each of the four coal samples as well as the diffractograms of the samples spiked with a material of known amorphous fraction content. For the latter, pure silicon was used to spike the samples.

This was followed by the combination of the two resulting spiked- and raw diffractograms to account for any shift of peaks and corrections. In addition, $K\alpha_2$ stripping was conducted in order to obtain the diffractograms only dependent on $K\alpha_1$ radiation. The X'Pert Highscore plus software was utilized to correct the final diffractograms for any polarisation- or geometrical effects (Franklin, 1951; Okolo, 2010; Lu *et al*., 2001). In addition, the absorption factor $A(\theta)$ was also corrected by using the Milberg equation as reported in literature (Okolo, 2010; Shiraishi & Kobayashi, 1973). After processing the diffractograms the different carbon crystallite parameters were respectively calculated. The interlayer spacing between aromatic sheets, d_{002}, of each coal was estimated using Braggs Law, which is defined as (Okolo, 2010; Takagi *et al*., 2004; Van Niekerk, 2008):

$$d_{002} = \frac{\lambda}{2 \sin \theta_{002}}$$ Equation (5.9)

Table 5.2 Summary of apparatus settings and parameters for carbon crystallite analyses.

Parameter or setting	*Description*
Anode material	Cobalt, Co target
Generator settings	45 mA, 35 kV
Angle of scan (°2θ)	4.0°< 2θ <120.0°
Kα1 (Å)	1.78901
$K\alpha_2$ (Å)	1.7929
K_β (Å)	1.62083
$K\alpha_2$-$K\alpha_1$ ratio	0.5
Step size (°2θ)	0.017
Scan step time (s)	13.335
Scan type	Continuous
PSD Mode	Scanning
PSD length (°2θ)	2.12
Divergence slit type	Programmable
Divergence slit size (mm)	15
Specimen length (mm)	10
Measurement Temperature (°C)	25
Spinning	Yes

The Scherrer equations as defined in Equation (5.10) and (5.11) were applied in order to respectively calculate the crystallite height (L_c) and average crystallite diameter ($L_{a,10}$) of each of the four coals (Feng *et al.*, 2003; Okolo, 2010; Takagi *et al.*, 2004; Van Niekerk, 2008; Wu *et al.*, 2008).

$$L_c = \frac{K\lambda}{\beta_{002}\cos\theta_{002}} \qquad \text{Equation (5.10)}$$

$$L_{a,10} = \frac{K\lambda}{\beta_{100}\cos\theta_{10}} \qquad \text{Equation (5.11)}$$

The average number of layers per carbon crystallite (N_{ave}) was calculated from the crystallite height and interlayer spacing with the use of Equation (5.12) (Trejo *et al*., 2007; Van Niekerk, 2008):

$$N_{ave} = 1 + \frac{L_c}{d_{002}} \qquad \text{Equation (5.12)}$$

Other structural parameters such as the fraction of amorphous carbon (X_A), the aromaticity (f_a) and the degree of disorder index (*DOI*) could also be determined from the corrected diffractograms. The smoothed and background subtracted diffractograms were baseline corrected with the use of the Origin 8.0 data processing package prior to the estimation of the fraction of amorphous carbon and aromaticity. The asymmetric nature of the characteristic d_{002} peak is believed to be the direct result of the complexity of the carbonaceous part of coals or coal chars (Wu *et al*., 2008). For this particular reason the normalized XRD diffractograms were de-convoluted into two main Gaussian curves representing the poor crystalline component (amorphous fraction), mainly reflected under the γ band of the diffractogram, and the relatively good crystalline component (graphitic- and turbostratic components) (Oya *et al.,* 1979; Wang *et al*., 2001; Wu *et al*., 2008).

Origin 8.0 was used to assist in the determination of the Gaussian curves. It is, however, assumed further that the fraction of amorphous carbon does not contribute to peak intensity but is only reflected in the background (Franklin, 1951; Ergun & Tiensuu, 1959; Lu *et al*., 2001). The fraction of amorphous carbon could therefore be estimated with relative ease from the different areas under the Gaussian curves by the following equation (Wu *et al*., 2008):

$$X_A = \frac{S_A}{S_A + S_G} \qquad \text{Equation (5.13)}$$

Similar to the fraction of amorphous carbon, the aromaticity of all four coals was calculated from the respective areas under the d_{002} and γ peaks by the following equation (Lu *et al*., 2001; Okolo, 2010; Trejo *et al*., 2007; Van Niekerk, 2008):

$$f_a = \frac{S_{002}}{S_{002} + S_\gamma}$$ Equation (5.14)

Finally the degree of disorder index (*DOI*) could be calculated from X_A and f_a by applying Equation (5.15) (Lu *et al.*, 2002):

$$DOI = X_A + (1 - X_A)(1 - f_a)$$ Equation (5.15)

5.3.1.4 Laser Desorption Ionization Time-of-Flight Mass Spectrometry (MALDI-TOF MS)

MALDI-TOF mass spectrometry was conducted on all four coal samples at Pennsylvania State University using a Micromass MALDI L/R linear and reflector mode mass spectrometer equipped with a nitrogen UV laser (337 nm wavelength). A similar experimental approach as described by Van Niekerk (2008) was used for this investigation. Raw (un-demineralised) coal samples with a particle size of less than 75 µm were sent for the analyses. Small amounts of the ultrafine coal samples were drawn up with a pipette tip and mixed with MilliQ water. The finely dispersed slurry was applied to the sample plate and the MilliQ water was left to evaporate from the plate in order to deposit the coal sample onto the sample target. Only reflector mode analyses were conducted by using a reflectron mode pulse voltage of 2300 V, a source voltage of 15000 V and a reflectron voltage of 2000 V (Van Niekerk, 2008). Each analysis was performed at a laser-firing rate of 5 Hz by taking 10 shots on different locations on the sample. The spectra was obtained in reflector mode and subsequently baseline corrected. Compounds below 70 m/z were not analysed due to the fact the high abundance of these chemical species could over-saturate the detector (Van Niekerk, 2008).

5.3.1.5 High-resolution transmission electron microscopy (HRTEM) and image analyses

Image acquisition

Coal samples with a particle size range of smaller than 75 µm were hand-ground for 15 minutes with a pestle and mortar in order to produce an ultrafine powdered sample. The finely ground

samples were suspended in acetone, whereafter 3 µl of the diluted mixture was applied to a 300 mesh Quantifoil R2/2 holey carbon copper grid by blotting and allowing the acetone to evaporate. The samples were viewed at 200 kV using a Tecnai F20 FEGTEM and photographed using a Gatan CCD camera (Model 895). The minimum dose method of observation was used as the samples were found to be beam sensitive. Essentially three modes were applied for obtaining the required images: search, focus and exposure. During search mode, the grids were scanned at low magnification (6500x) to find a thin enough layer or layers of particles that were situated at least partially across the holes in the carbon film. This was done in order to avoid the superposition of fringes due to the overlapping of multiple layers. Focus mode was only activated once a thin enough single layer was identified to be photographed. The image was subsequently focussed on an area, 0.15 µm away from it. The same magnification (700 000x) at which the photography took place was used. After focussing and correcting for astigmatism, exposure mode was chosen and the image was captured at -100 nm under focus. An exposure time of 1 second was used. After image acquisition the images were saved in dm3 format (Digital Micrograph) and converted to tif-format for lattice fringe analysis.

Lattice fringe image processing and analyses:

Obtained HRTEM images were subjected to image processing and analyses by utilizing the Image Processing Toolkit from Reindeer Graphics in conjunction with Adobe Photoshop CS5 software. A similar image processing methodology to that proposed in literature (Mathews *et al*., 2010; Sharma *et al*., 1999) was followed to extract and analyse the different lattice fringes. An overall schematic representation of the image analysis process is provided in Figure 5.1. Only images with an acceptable resolution were used for image processing. HRTEM images of each coal were imported into Adobe Photoshop CS5 in tif-format, whereafter it was converted to gray-scale and reset to a size of 4096 x 4096 pixels. The cropping tool in Photoshop CS5 was then applied to crop a particular random section in the original gray scale image. The same cropping size was used to crop the scale bar in order to determine appropriate scaling conversion after image analyses. The cropped section was automatically re-adjusted to a pixel size of 4096 x 4096 and was subsequently Fast Fourier Transformed with the help of the FFT (Forward) tool in the Image Processing Toolkit.

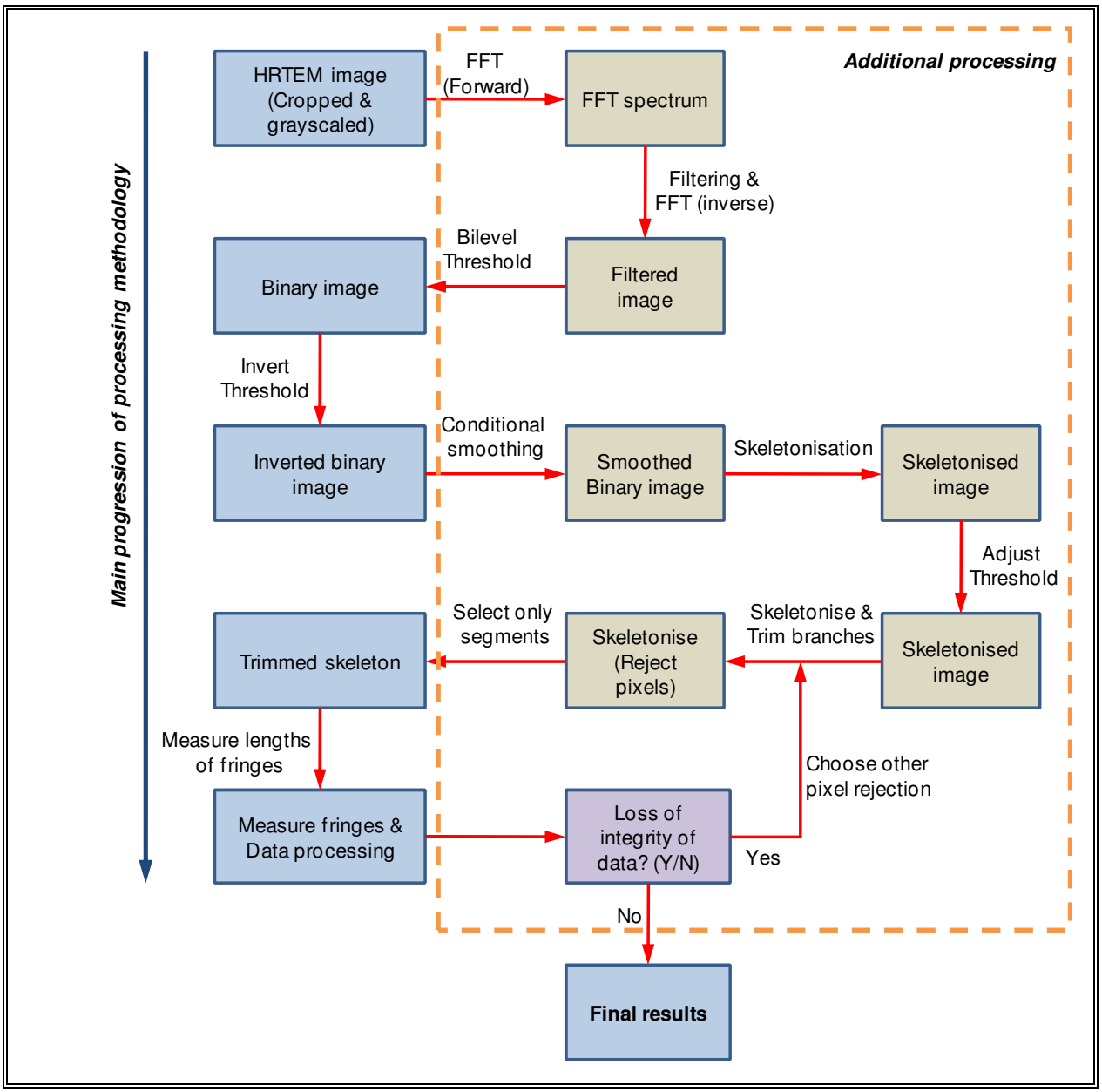

Figure 5.1 HRTEM image processing methodology.

This was followed by filtering the obtained Fourier spectrum with the application of the "ideal inverse" filtering option from the Image Processing Toolkit. The filtered Fourier spectrum was converted back to a filtered image format through application of inverse FFT. Furthermore, image resolution could also be additionally improved with the aid of the HDR toning tool in Adobe CS5. Analysis of the different lattice fringes requires that the filtered gray scale image be converted to a binary format. This was accomplished by applying the default threshold value to the image and inverting the obtained threshold image to obtain a black and white representation

of the original cropped image. Hereafter the inverted binary image was subjected to an additional smoothing step to remove any rough edges from the representative fringes in an attempt to avoid disturbances in the skeletonisation process. The conditional smoothing option in the Image Processing Toolkit was used for this purpose. After smoothing the inverted binary image, the skeletonisation feature was used to convert the image to a skeletonised representation of the fringes. The obtained skeletonised image was subjected to additional thresholding to differentiate smaller pixels, in the form of nodes, endpoints and branches, from the desired fringes. This was followed by a second application of skeletonisation, which included trimming the branches. The "skeletonise and trim branches" feature in the image processing toolkit was used to accomplish this.

The pixel rejection value of the trim branches option was varied between 5 and 80 pixels until an optimum value was reached. This was done to prevent the process of discarding lower fringe length entities such as benzene and naphthalene structures. Finally, the processed fringes were selected from the skeletonised image, after all possible nodes in the form of "Y" and "T" structures and endpoints were removed. The select skeleton components feature was used for this purpose, therefore discarding all the unnecessary nodes and endpoints. Once the skeletonisation process was successfully completed, the length of all the fringes were measured automatically by the image processing toolkit software. Fringe length data was processed and the integrity of the data was assessed by evaluating the presence of small fringe entities such as benzene or naphthalene structures. If integrity of the results were lost, the process of skeletonisation and trimming branches was repeated by choosing a different pixel cut-off value. This process was repeated until the optimum pixel rejection value was obtained. The final obtained results were subjected to additional lattice fringe analyses in order to determine the aromatic raft size distributions for all four coals.

Determination of the aromatic raft size distribution:

Multiple HRTEM images were cropped to extract the fringe representations of each coal. More than a 1000 fringes were processed and analysed to obtain the relevant aromatic raft size distributions. For this particular process the obtained fringes refer to only the aromatic portion of the coal structure and do therefore not take the hydrogen atoms and aliphatic carbons directly bonded to these aromatic sheets into account (Mathews *et al.*, 2010). Furthermore, the carbon ring catenation and angle of viewing play an important role in estimating the length of each

fringe. For this purpose, cut-off length values were used to differentiate between different low molecular weight aromatic structures such as benzene (<3 Å), naphthalene (<4.4 Å) and anthracene/phenanthrene (<5.9 Å). Aromatic ring structures containing more than 3 aromatic rings were, however, assumed to be in the form of parallelogram shaped aromatic rafts (Mathews *et al*., 2010; Van Niekerk, 2008). Aromatic raft structures ranging from 2x2 to 20x20 raft structures were constructed with the aid of the Accelrys Material Studio 5.0 molecular modelling package (Roberts, 2012). The molecular modelled representations were used to measure the minimum and maximum length of each aromatic raft. These parameters were applied further in the estimation of the molecular composition of each aromatic raft and in the classification of the different fringes from image analysis (Mathews *et al*., 2010; Roberts, 2012; Van Niekerk, 2008).

5.4 Results and discussion

5.4.1 Advanced analyses

5.4.1.1 Additional sample preparation

The outcome of the demineralisation procedure is reflected in the proximate results given in Table 5.3. The Table includes the effectiveness of demineralisation which can be defined as the difference between the original ash value ($m_{ash,raw}$ d.b.) and the demineralised coal ash value ($m_{ash,dem}$, d.b.), divided by the original ash value. Mathematically it can be expressed as:

$$\eta_{dem.} = 100 \times \left(\frac{m_{ash,raw} - m_{ash,dem.}}{m_{ash,raw}} \right) \qquad \text{Equation (5.16)}$$

It is evident from the results that the initial ash yields were substantially decreased from values of between 13.5 wt.% (d.b.) and 18.6 wt.% (d.b.) to final ash yield values of lower than 3 wt.% (d.b.), indicating that the process of demineralisation was indeed successful. Demineralisation effectiveness also reported values of higher than 85%. Furthermore, it can be observed that the fixed carbon content of each coal increased significantly after demineralization. This was, however, not the case for the volatile matter content, with values for both raw- and

demineralised coal samples (with the values of coals INY and UMZ slightly lower) staying approximately constant. The similarity in volatile matter content indicates to some extent that structural transformations of organic matter could have possibly occurred during the demineralization process.

Table 5.3 Proximate analysis comparison between raw- and demineralised coal samples.

Coal sample		*Volatile matter (wt.% d.b.)*	*Fixed Carbon (wt.% d.b.)*	*Ash content (wt.% d.b.)*	*Effectiveness, $\eta_{dem.}$ (%)*
INY	Raw	25.5	55.9	18.6	85.5
	Demineralised	25.1	72.2	2.7	
UMZ	Raw	25.2	59.6	15.2	92.1
	Demineralised	24.4	74.3	1.2	
G#5	Raw	34.1	52.4	13.5	88.9
	Demineralised	34.5	64.0	1.5	
TSH	Raw	20.5	61.7	17.8	96.6
	Demineralised	21.8	77.6	0.6	

Slight increases in volatile matter contents were, however, observed for coals G#5 and TSH. Similar observations were made by Lu *et al*. (2001) and Van Niekerk (2008).

5.4.1.2 Solid-state ^{13}C nuclear magnetic resonance spectroscopy (^{13}C NMR)

All four coals were subjected to CP-MAS- and DD NMR experiments in order to obtain a semi-quantitative estimation of their respective structures. The experimental methodology is provided in Section 5.3.1.2. It is well known that the reliable accuracy of CP-MAS can be an issue due to the fact that this method discriminates against aromatic carbon atoms (Van Niekerk, 2008). For increased accuracy in the results, single pulse excitation magic-angle-spinning (SPE-MAS) NMR experiments are normally proposed (Botto *et al*., 1987; Franz *et al*., 1992; Muntean *et al*., 1988; Van Niekerk, 2008), but due to its excessively time consuming nature the CP-MAS technique is normally preferred. Variable contact time- and dipolar dephasing experiments do however provide additional assistance with the reliability of the determined aromatic values (Orent *et al*., 1992; Solum *et al*., 1989; Solum *et al*., 2001). Numerous authors including Miknis

et al. (1988), Perry *et al.* (2000), Solum *et al*. (1989 & 2001), Van Niekerk (2008) and Watt *et al*. (1996) have applied the CP-MAS and DD-MAS techniques for establishing a semi-quantitative description of the carbon-matrix of coal. The ^{13}C CP-MAS spectra obtained for each coal, as well as the integral reset points, are provided in Figures 5.2 to 5.5.

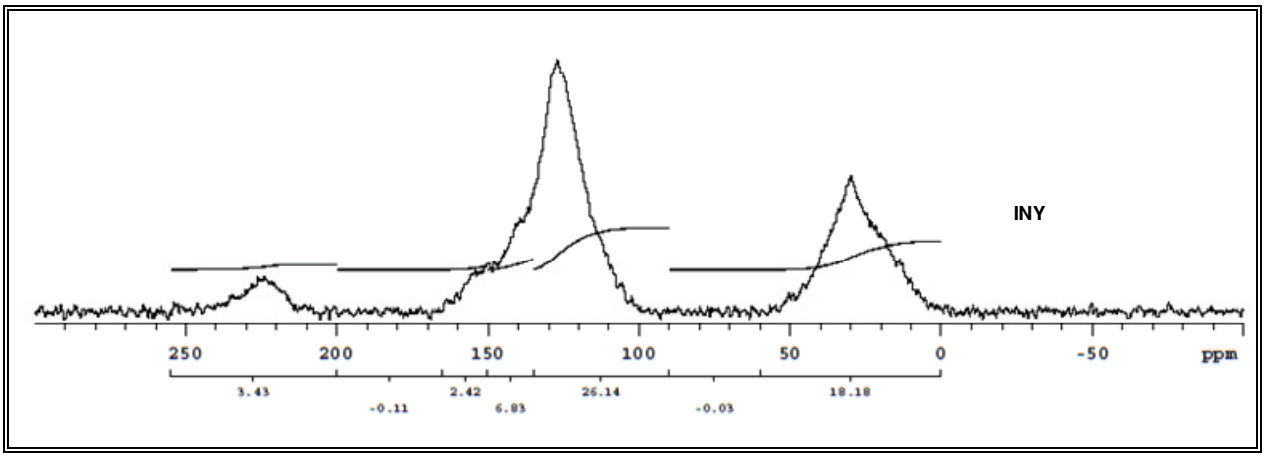

Figure 5.2 CP-MAS acquired spectra for coal INY.

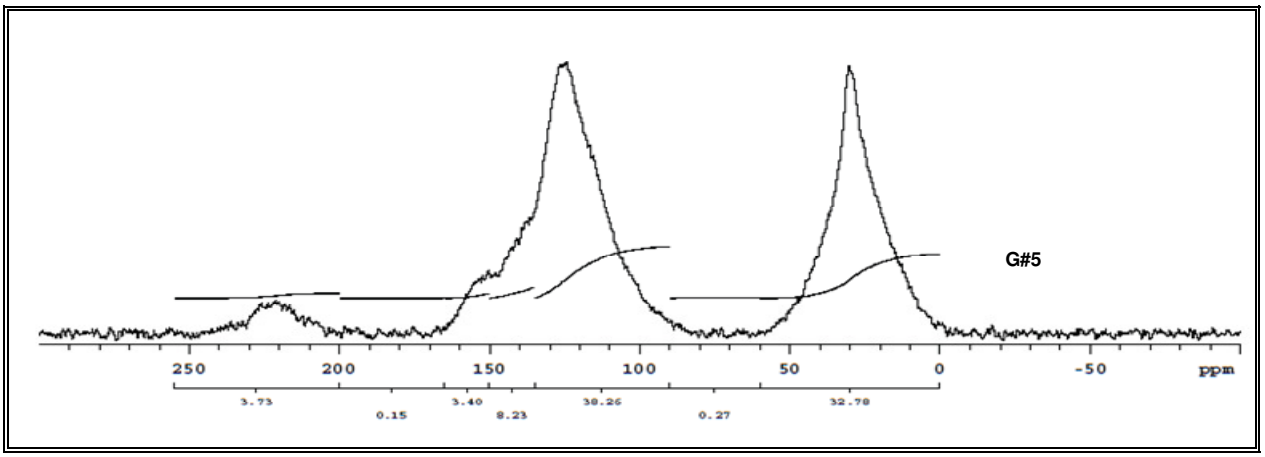

Figure 5.3 CP-MAS acquired spectra for coal G#5.

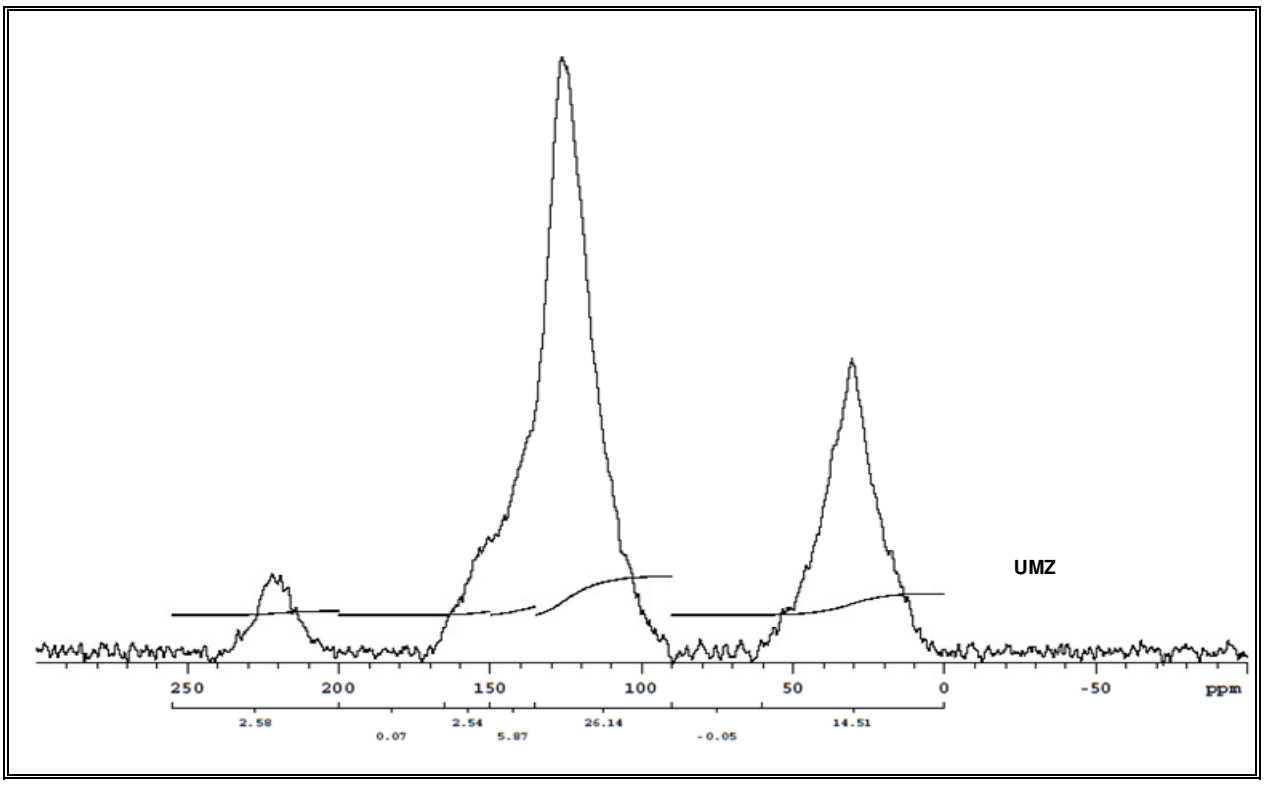

Figure 5.4 CP-MAS acquired spectra for coal UMZ.

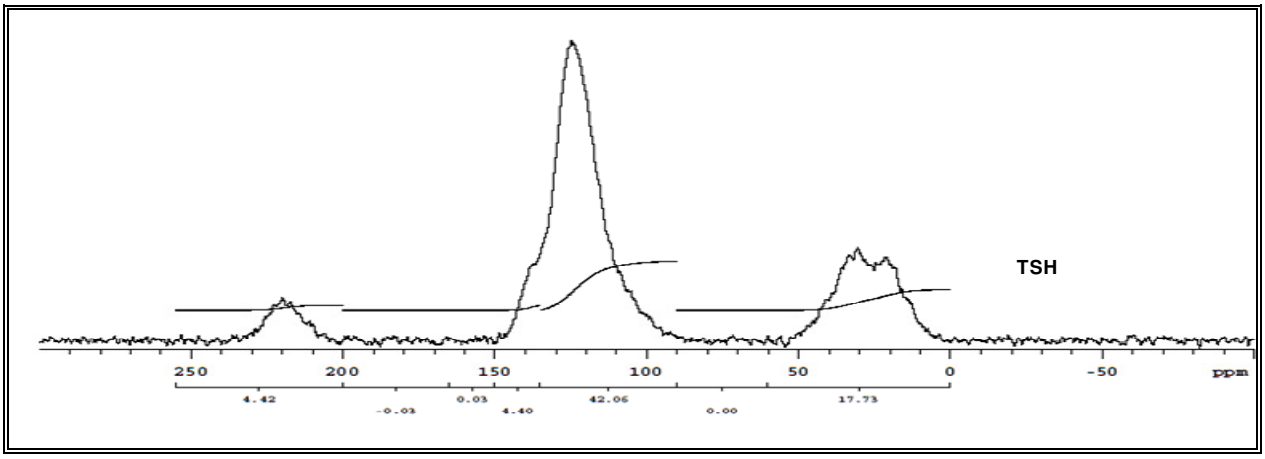

Figure 5.5 CP-MAS acquired spectra for coal TSH.

From the above figures it is evident that the CP-MAS spectra of all four coals exhibit three distinct peaks: a less prominent spinning sideband peak at 200-255 ppm, an aromatic region at 90-200 ppm and an aliphatic region at 0-90 ppm. Qualitatively, the aromatic- and aliphatic peaks of coals INY and UMZ are quite similar, whereas both the aromatic- and aliphatic peaks of coal G#5 are similar in height. The main spectral areas (aromatic and aliphatic) can be further subdivided into smaller carbon specific regions as illustrated for the spectra of coal G#5 in

Figure 5.6. The annotations of the carbon specific species in Figure 4.14 were done in accordance with Solum *et al.* (1989) and Suggate and Dickinson (2004).

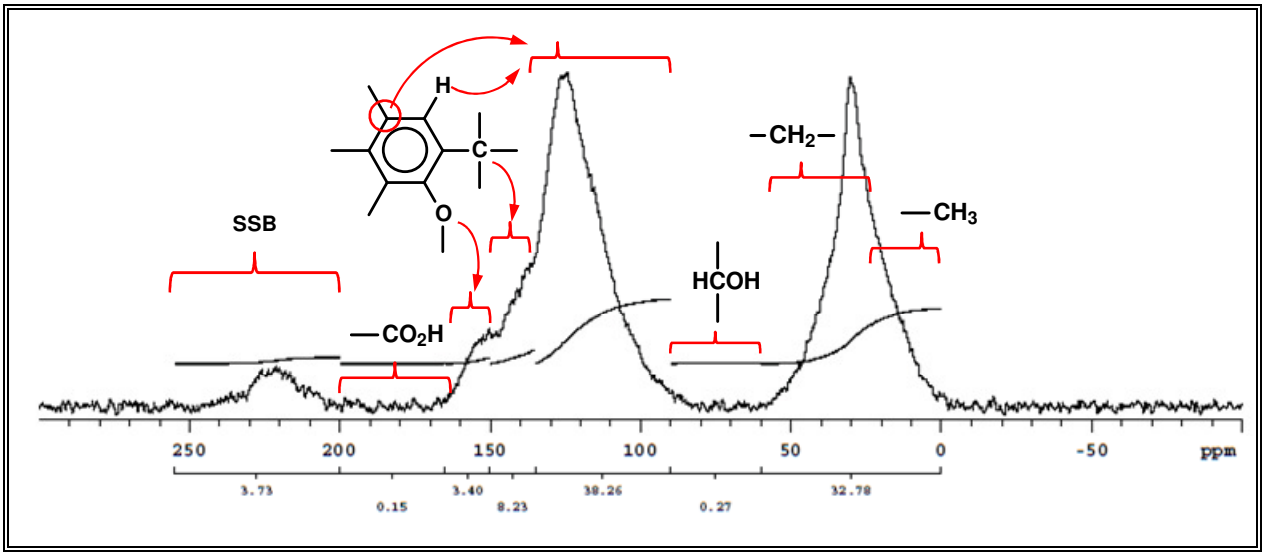

Figure 5.6 Annotated CP-MAS spectra of coal G#5 (According to Suggate & Dickinson (2004)).

Table 5.4 summarises the chemical shift values of the different subsections of the CP-MAS spectrum (Assumption, 2010; Solum *et al.*, 1989 & 2001).

Table 5.4 Summary of sub-sections of main spectral areas.

Chemical shift range (δ, ppm)	*Symbol*	*Main spectral region*	*Sub-spectral region*
200-165	f_a^C	Aromatic	Carbonyl / Carboxyl functionalities in the form of acids, esters, amides.
165-150	f_a^P	Aromatic	Phenolic functionalities in the form of phenols and phenolic ethers.
150-135	f_a^S	Aromatic	Alkylated compounds
135-90	f_a	Aromatic	Aromatic C + CH
90-60	f_a^O	Aliphatic	Aliphatic C connected to O
60-0	f_{al}	Aliphatic	Aliphatic functionalities in the form of methyl and methoxy methyl groups.

The structural- and lattice parameter results (as described in Section 5.3.1.2) are provided respectively in Tables 5.5 and 5.6.

Table 5.5 Structural parameters from ^{13}C NMR for all four coals.

Structural parameter	*COALS*				*Ranges from literature***
	INY	*UMZ*	*G#5*	*TSH*	
f_a	0.74	0.77	0.66	0.81	**0.60-0.86**
f_a^C	< 0.01	< 0.01	< 0.01	0.00	**0.00-0.10**
$f_{a'}$	0.74	0.77	0.66	0.81	**0.53-0.86**
f_a^H	0.23	0.29	0.24	0.33	**0.16-0.33**
f_a^N	0.51	0.48	0.42	0.48	**0.28-0.54**
f_a^P	0.05	0.06	0.04	<< 0.01	**0.02-0.09**
f_a^S	0.14	0.13	0.11	0.08	**0.13-0.21**
f_a^B	0.32	0.29	0.26	0.40	**0.09-0.34**
f_{al}	0.26	0.23	0.34	0.19	**0.14-0.40**
f_{al}^H	0.22	0.20	0.28	0.12	**0.08-0.29**
f_{al}^*	0.04	0.03	0.06	0.07	**0.06-0.17**
f_{al}^O	< 0.01	0.00	< 0.01	<< 0.01	**0.01-0.12**

***Literature ranges taken from Solum et al. (1989 & 2001), Van der Merwe (2010), Van Niekerk (2008) and Watt et al. (1996.)*

An appreciable difference could be observed between the fraction of aromatics (f_a) of the four coals, with coal TSH exhibiting a highly aromatic nature with respect to the other coals. Coal G#5 only contained about 66% aromatics, making it the least aromatic coal of the four. DD experiments were also conducted in order to differentiate between protonated and non-protonated aromatic- and aliphatic carbon entities. The spectra obtained from these experiments are provided in Appendix B.1. No significant variance was observed between the amounts of carbonyl (f_a^C), non-protonated (f_a^N)- and alkylated (f_a^S) aromatic carbons, which also holds true for the amount of oxygenated and non-protonated aliphatic species (f_{al}^O,f_{al}^*). Carbonyl species in the form of esters, acids or amides were, however, not observed for coals UMZ and

TSH, whereas only negligible amounts of smaller than 1% were observed for the other two coals. The largest differences in molecular carbon structure were observed for coals G#5 and TSH, while coals UMZ and INY exhibited quite comparable results with only slight differences between some structural parameters. Of all four coals, coal TSH contained the highest amount of protonated aromatic carbons (33%), the lowest amount of protonated aliphatic carbon (12%) and essentially no phenolic aromatic- and oxygenated aliphatic carbons. The negligible amounts of O functionalities in coal TSH is in agreement with the significantly low elemental O value obtained from the ultimate analysis. In addition, coal TSH had the largest bridgehead value (40%), indicating a more poly-condensed aromatic structure for this coal, which is also evident from the large fixed carbon (75.1 wt.% d.a.f.) value obtained from proximate analysis. The higher poly-condensed structure of coal TSH is also reflected in the decreasing trend observed between the fractional amount of aromatics and the atomic O/C ratio (a rank dependent parameter) as seen in Figure 5.7. Coal G#5, however, is characterised by its substantially larger aliphatic content, which contains a larger proportion of protonated carbons in comparison to the other three coals.

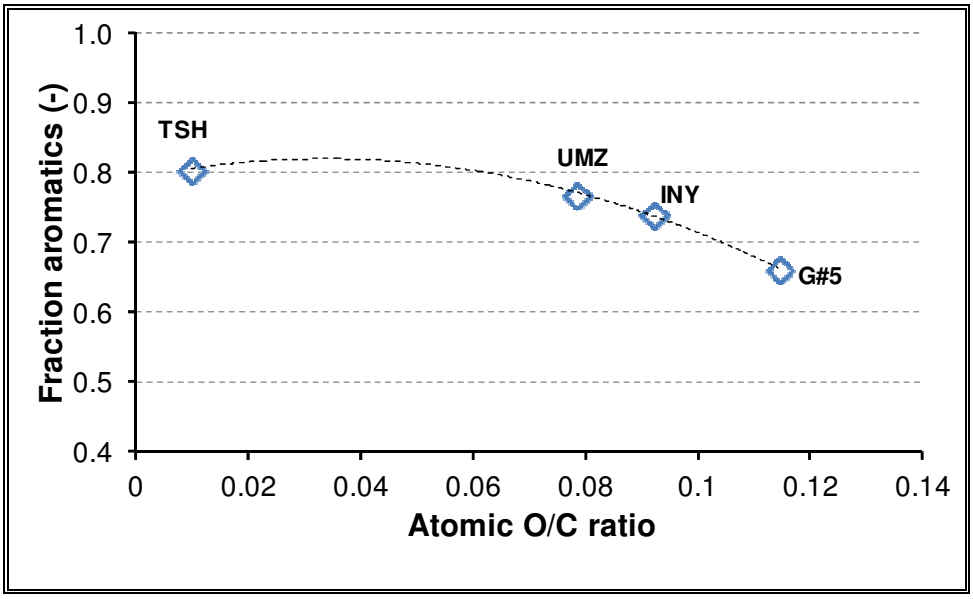

Figure 5.7 Correlation between fraction aromatics and atomic O/C ratio.

It has been generally established that aromaticity increases with increasing coal rank (Smith *et al.*, 1994; Solum *et al.*, 1989). Although all four coals were classified as medium rank bituminous coals, the difference in aromaticity can also be related to the reflectance of the vitrinite macerals of each coal as graphically illustrated in Figure 5.8.

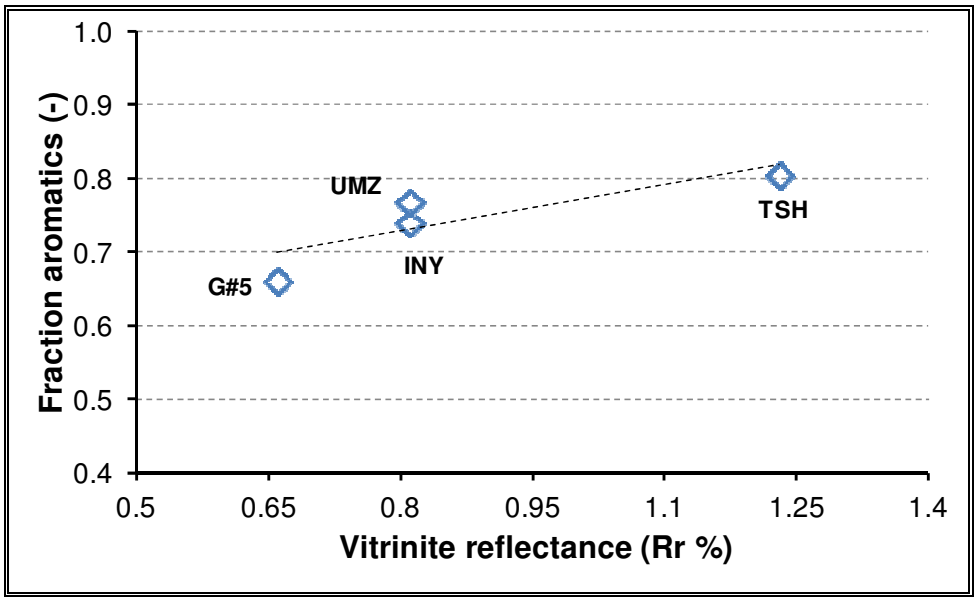

Figure 5.8 Correlation between fraction aromatics and vitrinite reflectance.

It is clear from the Figure that coal aromaticity increases with increasing vitrinite reflectance. This indicates that the highly condensed nature of coal TSH can be attributed to its elevated level of vitrinite maturity with respect to the other three coals. As a comparison, Table 5.5 also includes some specified CP-MAS values obtained from literature. It is clear that the structural values obtained in this investigation show good agreement with published results. The calculated lattice parameters (as discussed in Section 5.3.1.2.) of the coals are summarised in Table 5.6.

Table 5.6 NMR derived lattice parameters for the four coals.

Coal	χ_b	*C*	$\sigma+1$	P_0	*B.L.*	*S.C.*	*MW*	M_δ
INY	0.43	21	5.5	0.80	4.4	1.1	419	29.2
UMZ	0.38	19	4.6	0.85	3.9	0.7	348	25.7
G#5	0.40	20	4.6	0.62	2.8	1.7	448	45.1
TSH	0.50	24	2.3	0.09	0.2	2.1	400	41.9
Ranges from literature*	**0.17 - 0.40**	**9 - 20**	**3.2 - 5.9**	**0.48 - 0.84**	**2.3 - 4.5**	**0.8 - 2.5**	**251 - 459**	**24 - 42**

***Literature ranges taken from Solum et al. (1989 & 2001), Van der Merwe (2010), Van Niekerk (2008) and Watt et al. (1996.)*

The obtained lattice parameters provide valuable information regarding the average molecular structure of the four coals in terms of the average cluster size (*C*) and the number of attachments ($\sigma+1$). The number of attachments consists of the number of aliphatic side chains terminating in methyl groups (side chains-S.C.), the number of connections between clusters (bridges-B.L.) and connections back to the same cluster (loops-B.L.), respectively. Table 5.6 also includes the values determined for the mole fraction of bridgehead carbons (χ_b), the total molecular weight per cluster (*MW*) and the average molecular weight of a side chain or a half of the bridge mass (M_δ). The latter two parameters were estimated from correlations published by Solum *et al*. (2001). Figure 5.9 provides a graphical representation of the average cluster size, number of attachments and proposed average molecular cluster units of the four coals.

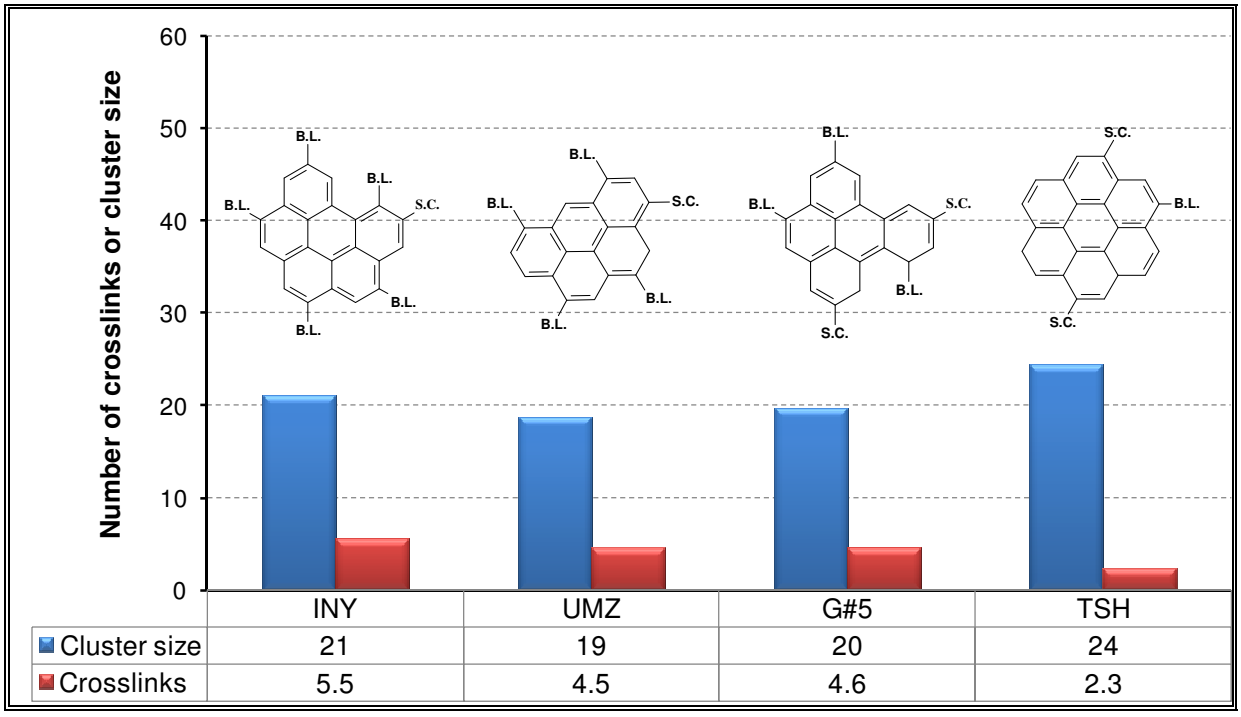

	INY	UMZ	G#5	TSH
Cluster size	21	19	20	24
Crosslinks	5.5	4.5	4.6	2.3

Figure 5.9 Average cluster size and attachments for the four coals.

From Table 5.6 and Figure 5.9 it can be seen that coals INY, UMZ and G#5 display similar cluster sizes, while only coal TSH contains a slightly higher amount of aromatic carbons per cluster (24 in this particular case) with respect to the other coals. The average molecular structures were estimated from the combined linear- and circular catenation models as described by Solum *et al*. (1989). It was therefore evident that the average molecular structures of coals INY, UMZ and G#5 are combinations of both linear- and circular catenation, whilst the structure of coal TSH can be largely estimated by circular catenation (coronene or

circumcoronene type of structures). Coals INY, UMZ and G#5 all contain at least 4 or 5 bridge or loop structures, whereas coal TSH is characterised by only one bridge or loop. The calculated *MW* and M_δ data indicates that coal UMZ has the lowest total molecular weight per cluster, while coals G#5 and TSH exhibit side chains or half bridges with large average molecular weights. This can possibly be attributed to long side chains or bridge-loop structures in comparison to the other coals.

5.4.1.3 X-ray diffraction (XRD)-carbon crystallite analyses

The raw diffractograms, corrected for polarisation and geometrical effects, of the four demineralised coal samples are provided in Figure 5.10. Careful examination of this Figure indicates the presence of high background intensity, which can be ascribed to the fact that not all the carbon present in coal is in aromatic form but can also propagate in amorphous form (Maity & Mukherjee, 2006). Figure 5.11 shows the processed and smoothened diffractograms after the background, due to the amorphous carbon fraction, was removed. Background subtraction and smoothening was accomplished with the help of the HighScore Plus peak analysis tool.

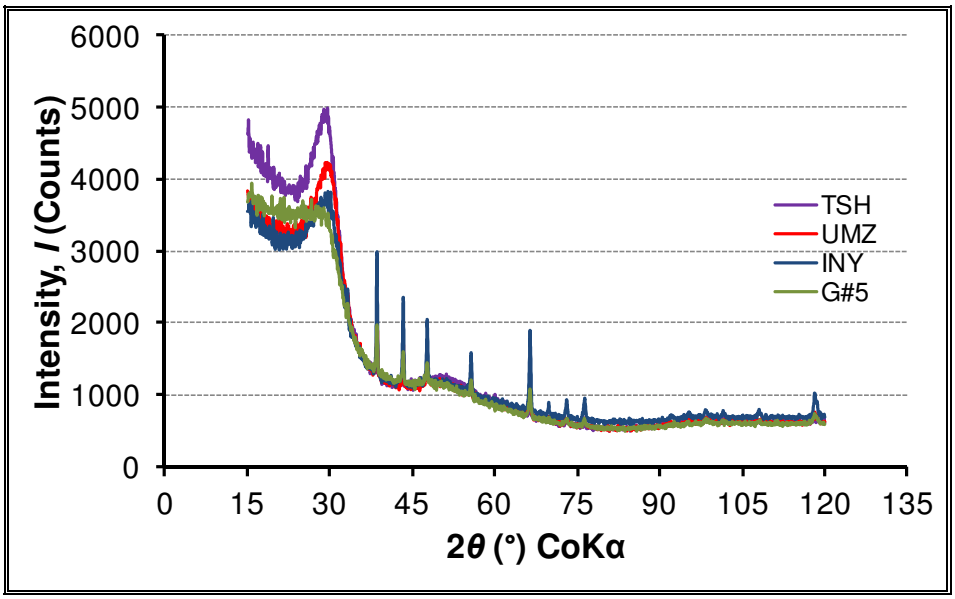

Figure 5.10 Raw diffractograms of the four coals.

The diffractograms as presented in Figures 5.10 and 5.11 display similar graphitic-like features as observed in numerous other carbon crystallite studies conducted on coal and char (Franklin, 1951; Lu *et al.*, 2001; Lu *et al.*, 2002; Maity & Mukherjee, 2006; Okolo, 2010; Shiraishi & Kobayashi, 1973; Wu *et al.*, 2008). All four coal samples were characterised by a distinct peak in the range of $27.6° < 2\theta < 29.3°$ as well as two less prominent peaks confined respectively to the ranges $38.8° < 2\theta < 56.3°$ and $89.5° < 2\theta < 104.1°$ (Okolo, 2010; Takagi *et al.*, 2004). The most prominent peak (Figure 5.11) corresponds to the (002) reflection of carbon due to the layer stacking of aromatic structures and can therefore be related to the interlayer spacing of graphite (Okolo, 2010; Takagi *et al.*, 2004). The other two peaks, respectively annotated as the (10) and (11) bands, correspond to the (*hk0*) lines of graphite, which can be related to hexagonal ring structures (Okolo, 2010).

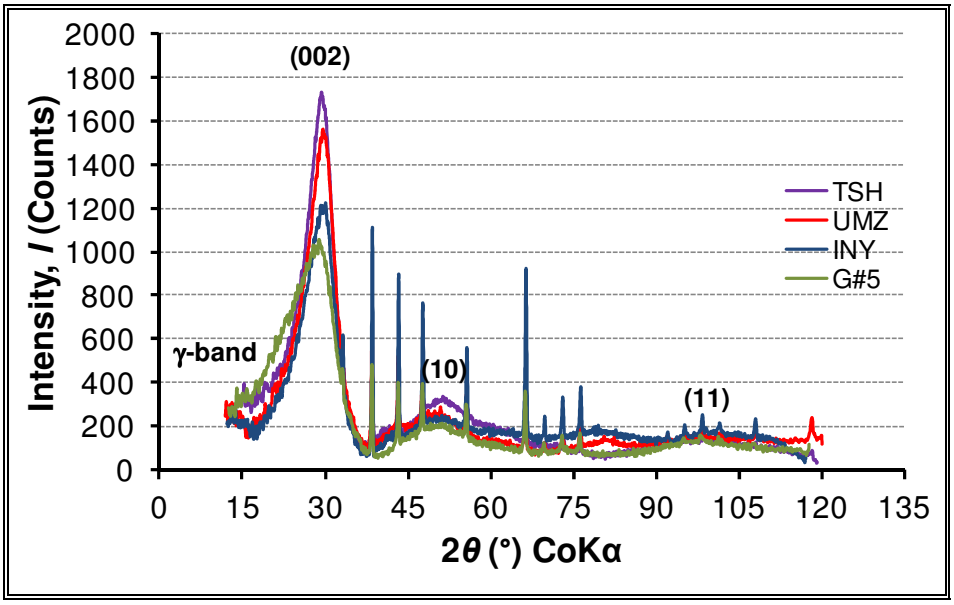

Figure 5.11 Corrected and smoothened diffractograms of the four coals.

From both Figures it is clear that coal TSH showed the highest intensity of the d_{002} band, followed by coals UMZ, INY and G#5. The descriptive sharp peaks for pyrite were also observed for coals UMZ, INY and G#5, which indicated the presence of un-removed pyrite within the demineralised coal structures. This did, however, not affect the determinations of the crystallite parameters, due to the fact that these peaks did not interfere or obscure the intensities of the (002) and (10) bands of the three coals. Theoretically the (002) band displays a symmetric profile (Lu *et al.*, 2001), but the apparent asymmetric nature of this peak as observed in Figure 5.11 has necessitated the need to delineate this peak into the d_{002} peak and

the γ-sideband (Ergun & Tiensuu, 1959; Franklin, 1951; Okolo, 2010). The existence of the γ-sideband can be associated with saturated organic structures such as aliphatic side chains, (Ergun & Tiensuu, 1959) and is assumed not to contribute to the high angle side of the d_{002} peak due to its low intensity (Lu *et al*., 2001). The calculated crystallite parameters from the corrected and smoothened diffractograms are presented in Table 5.7.

Table 5.7 Summary of crystallite parameters of the four coals.

Crystallite parameter	*Symbol*	*INY*	*UMZ*	*G#5*	*TSH*
Interlayer spacing (Å)	d_{002}	3.51	3.51	3.58	3.54
Stacking height (Å)	L_c	17.7	18.8	14.6	18.5
Stacking diameter (Å)	$L_{a,(10)}$	11.2	13.5	13	10.7
Average number of stacks	N_{ave}	6.05	6.36	5.07	6.23

The interlayer spacing was calculated by application of Bragg's law to the (002) peak position, while L_c and L_a were respectively calculated from the peak position and full width at half maximum (FWHM) of the (002) and (10) bands. The (11) band was, however, not used for quantitative analyses, due to its diffuse and obscure nature (Okolo, 2010). All four coals displayed inter planar distances comparable to graphite (d_{002} for artificial graphite is 3.36 to 3.37 Å, while the d_{002} for true graphite is known to be 3.354 Å) (Franklin, 1951; Iwashita & Inagaki, 1993; Lu *et al*., 2001). In addition, the average number of stacks (N_{ave}) was determined according to Equation (5.12). The influence of elemental C content (or rank of coal) on the interlayer spacing of the coal has generally been attended to in literature (Lu *et al*., 2001; Maity & Mukherjee, 2006; Takagi *et al*., 2004). No significant trend between elemental C content and interlayer spacing could be inferred, mainly due to only slight differences in the respective interlayer spacing values of these coals. This may be attributed to the fact that all four coals were quite similar in rank (Okolo, 2010). Significant differences could, however, be observed between the L_c and $L_{a,(10)}$ values of coal G#5 with respect to the other three coals. The lower L_c value of coal G#5 supports the fact that this coal has a less ordered structure when compared to the other three coals (Van Niekerk, 2008). This was also observed from the ^{13}C NMR results. The average number of crystallites in a stack was found to range between 5 and 7 for all the coals, with coal G#5 containing the lowest amount of these crystallites. The crystallite parameters as obtained for the four coals under investigation agree with results obtained in numerous other studies concerning carbon crystallite analyses of coals (Lu *et al*., 2001; Okolo, 2010; Takagi *et al*., 2004; Van Niekerk, 2008). The determination of the amount of amorphous carbon as well as the aromaticity involved additional processing of the corrected diffractograms.

The method proposed by Wu *et al*. (2008) and Wang *et al*. (2001) was used to estimate the amount of amorphous carbon. The application of this method has been briefly attended to in Section 5.3.1.3. The separated Gaussian curves as obtained from Origin 8.0 software as well as the original diffractogram of coal G#5 are presented in Figure 5.12. The deconvolution results of the other three coals are provided in Appendix B.2.

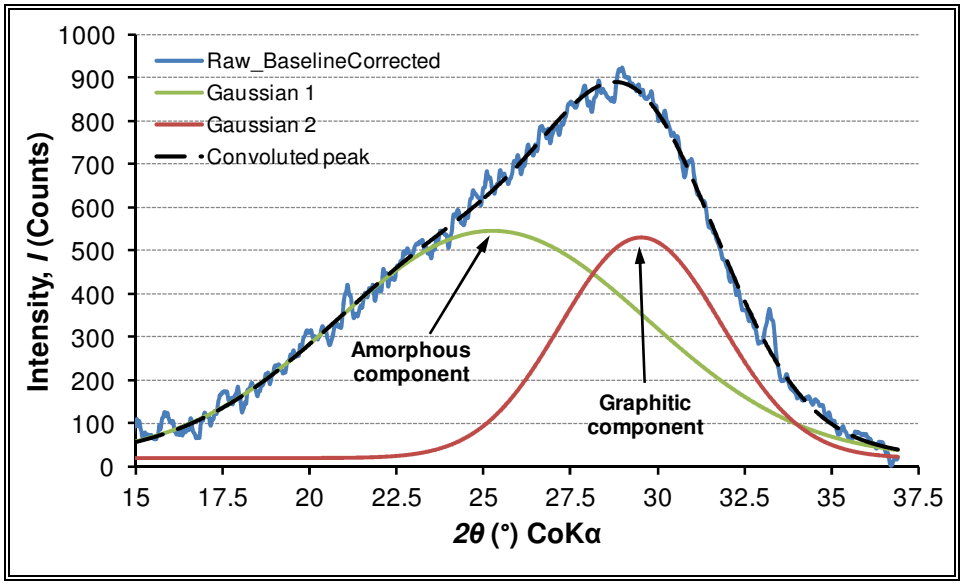

Figure 5.12 Determination of the fraction of amorphous carbon of coal G#5.

The fraction of amorphous carbon could therefore be calculated with relative ease from the respective areas under the two Gaussian curves by using Equation (5.13). The determination of the aromaticity of the four coals followed a similar deconvolution strategy but with some constraints. The high angle side of the (002) peak was used to symmetrically delineate the (002) band by assuming that the γ band does not contribute to the intensity of the high angle side (Lu *et al*., 2001). The delineation of the (002) band involved the fitting of a Gaussian curve to the high angle side of the peak and optimizing the Gaussian curve parameters to minimize the error sum of squares between the predicted values and the experimental values from the diffractogram. Once the Gaussian peak describing the (002) band was resolved, a second Gaussian curve was fitted to the remaining intensity in the low angle side of the peak and was therefore attributed to the γ band. The sum of the two Gaussian curves was calculated to obtain a convoluted peak that could describe the combined (002) and γ band. In addition, the error sum of squares between the predicted values of the convoluted peak and the experimental values from the diffractogram was minimized by optimizing the Gaussian curve parameters describing

the γband. After peak deconvolution, the respective areas under the (002) band and γband was used to estimate the aromaticity of each coal with the use of Equation (5.14). The deconvolution of the diffractogram of coal G#5 is presented in Figure 5.13. Deconvolution results for the other three coals are presented in Appendix B.3.

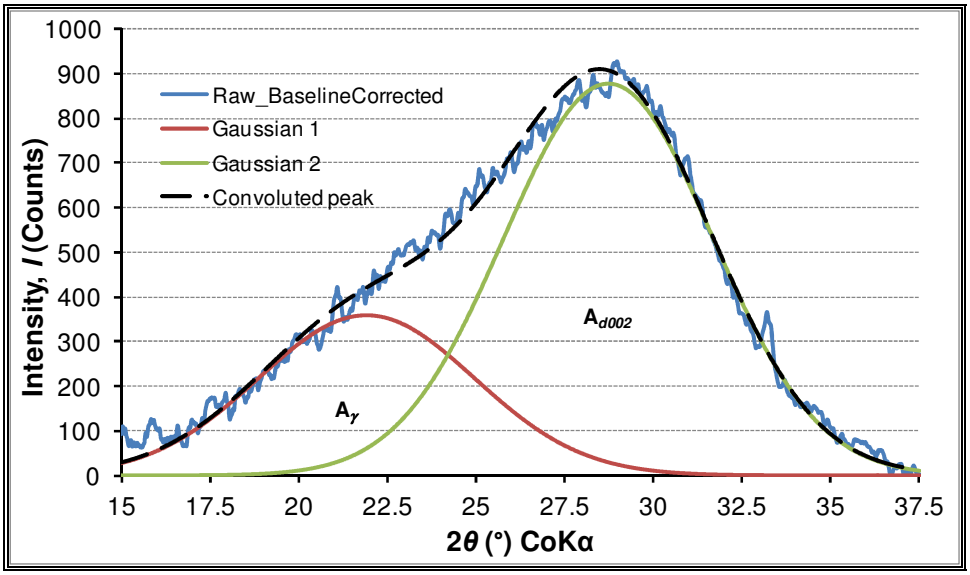

Figure 5.13 Determination of the aromaticity of coal G#5.

A confirmation of the aromaticity results were conducted using both the curve fitting analysis tool in HighScore Plus and Origin 8.0 data processing software. The degree of disorder index (*DOI*) was subsequently calculated from the obtained X_A and f_a values as discussed in Section 5.3.1.3. A comparison of the obtained results between the four different coals is provided in Table 5.8.

Table 5.8 Summary of additional crystallite parameters.

Crystallite parameter	*Symbol*	*INY*	*UMZ*	*G#5*	*TSH*
Fraction of amorphous carbon	X_A	0.58	0.59	0.67	0.52
Aromaticity*	f_a	0.75	0.76	0.68	0.82
Aromaticity**	f_a	0.80	0.79	0.70	0.86
Aromaticity***	f_a	0.76	0.80	0.63	0.83
Degree of disorder index	*DOI*	0.69	0.69	0.78	0.61

** As determined by Origin 8.0; ** As determined manually; *** As determined by Highscore Plus.*

From the Table it is clear that a good similarity exists between the aromaticity data obtained by the three data analyses applications. This is in agreement with what was found by Okolo (2010).

The obtained aromaticity results showed excellent agreement with what was obtained by ^{13}C NMR. Figure 5.14 shows the dependency of aromaticity on the atomic H/C ratios of the four coals.

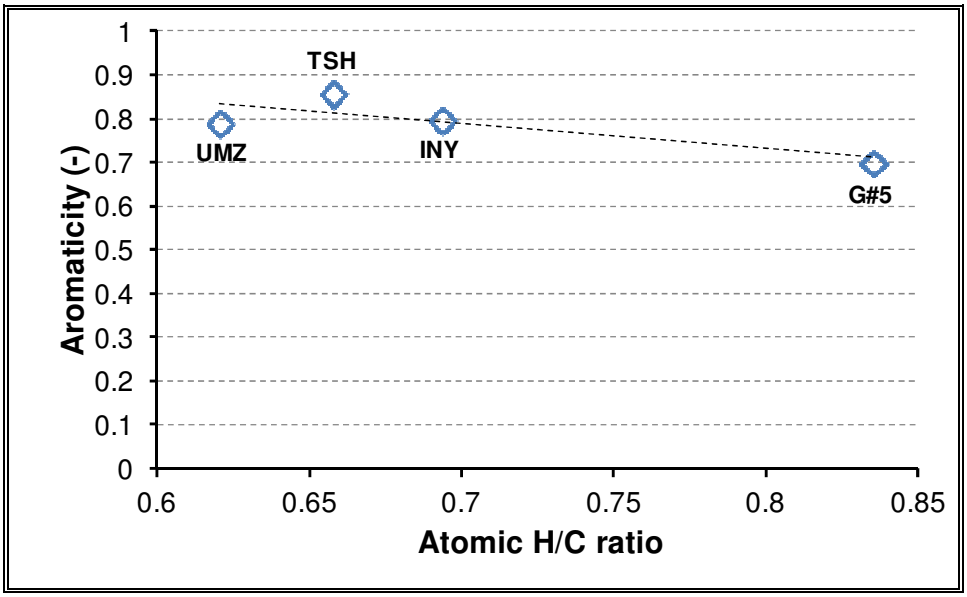

Figure 5.14 Dependency of aromaticity on atomic H/C ratio.

From the above Figure it can be seen that coal aromaticity decreases almost linearly with increasing H/C ratio, which can be attributed to the strong association of hydrogen functionalities with the low molecular aliphatic groups of the coal structure. An increase in the proportion of these groups will therefore result in a higher volatile matter content of the coal and a subsequent lower aromaticity (Choi *et al*., 1989; Okolo, 2010). The fraction of amorphous carbon provides an indication of the disordered material within the coal structure (Lu *et al*., 2001). The effect of the fraction of amorphous carbon and the degree of disorder index (*DOI*) on volatile matter content is displayed graphically in Figure 5.15. The amount of volatile matter (wt.% d.b.) increases with both an increase in the fraction of amorphous carbon and the *DOI*. Higher values of these two parameters are indicative of a higher relative abundance of disordered carbon (Lu *et al*., 2002; Okolo, 2010), possibly in the form of low molecular weight aliphatics and/or saturated hydrocarbons. This can possibly contribute largely to the amount of volatile matter released during devolatilization. The higher volatile matter content of coal G#5 can therefore be attributed to its less ordered structure (Okolo, 2010).

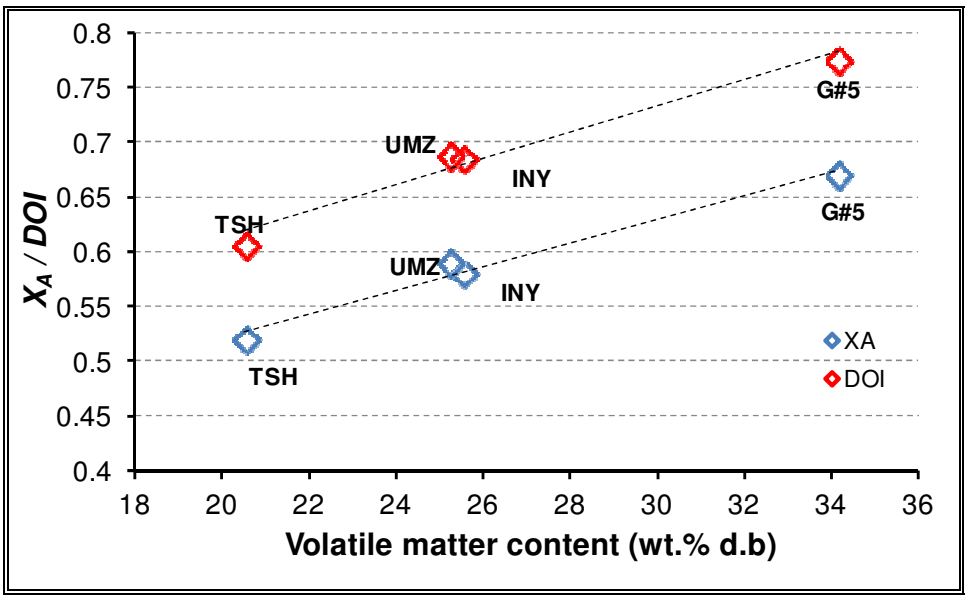

Figure 5.15 Influence of X_A and *DOI* on coal volatile matter.

The contribution of aliphatic functionalities (as taken from ^{13}C NMR), within the coals, to the overall order of the coal structures is also reflected in Figure 5.16.

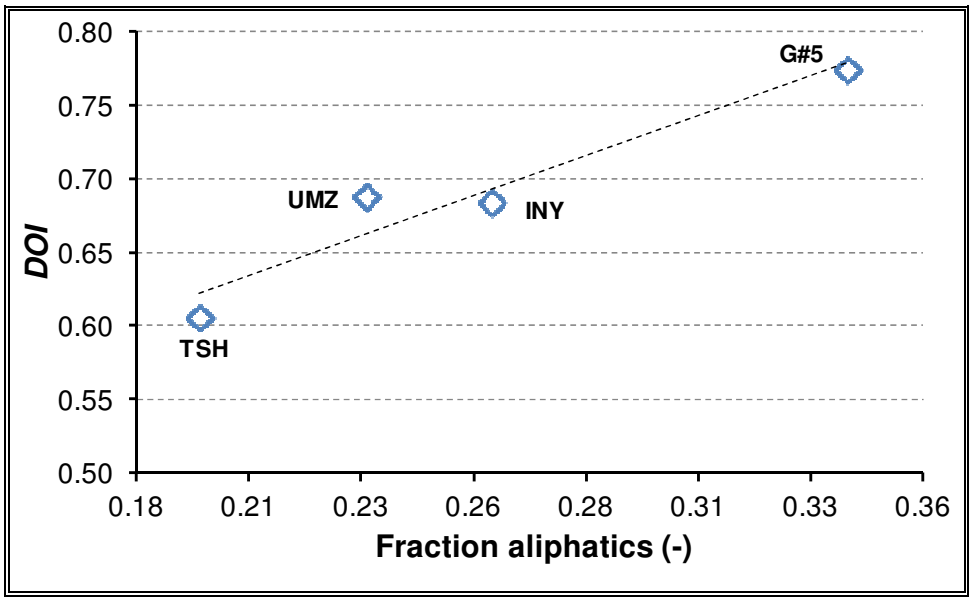

Figure 5.16 Influence of fraction of aliphatics on order of coal structure.

The fraction of aliphatics therefore contributes to a higher disorder in the molecular structure of coal G#5, whilst the structure of coal TSH tends to be more ordered (Okolo, 2010).

5.4.1.4 Laser Desorption Ionization Time-of-Flight Mass Spectrometry (MALDI-TOF MS)

Laser desorption ionization time-of-flight mass spectra were obtained in reflector mode (75 to 5000 m/z) for the four coal samples. The spectra obtained are provided respectively in Figures 5.17 and 5.18 for the inertinite-rich coals (UMZ and INY) and the vitrinite-rich coals (G#5 and TSH).

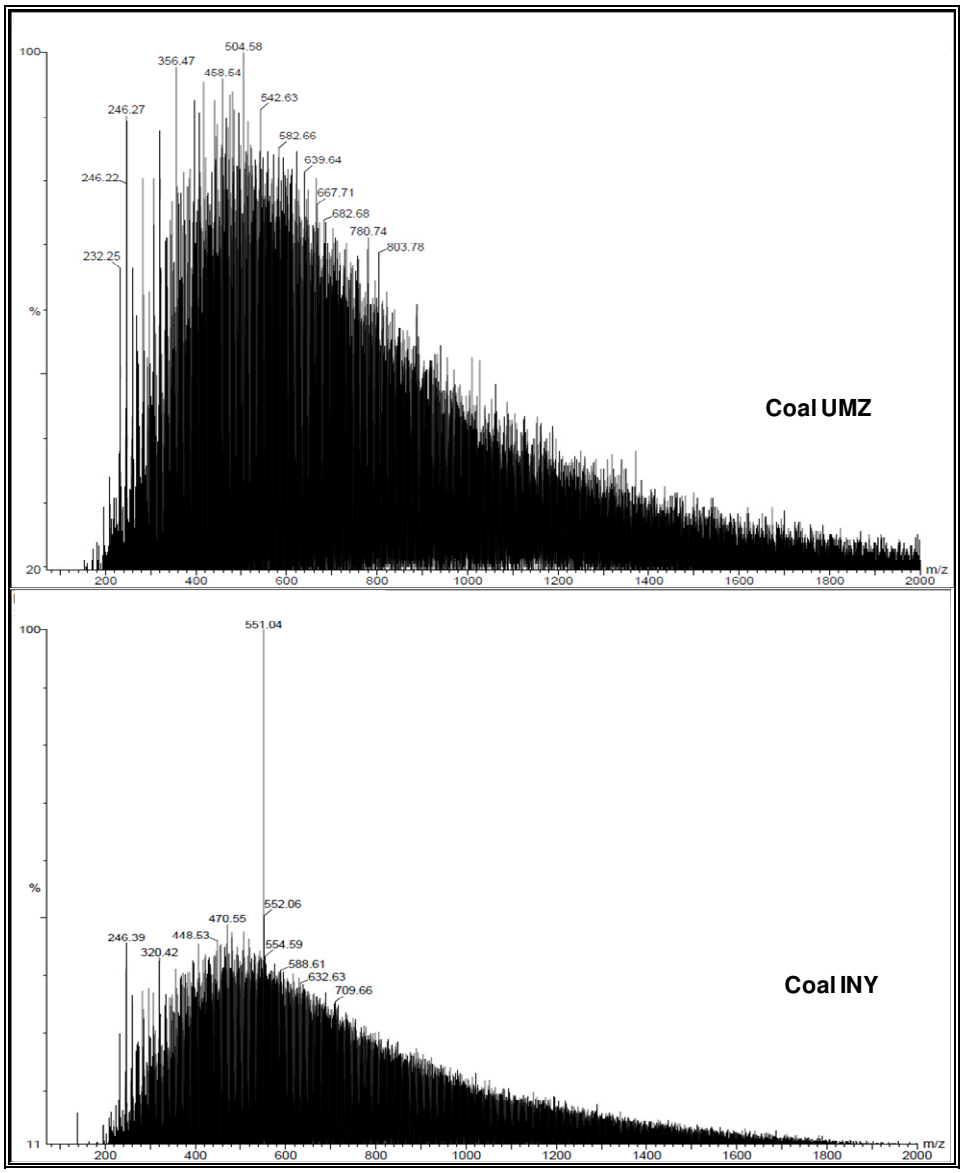

Figure 5.17 MALDI-TOF MS spectra of coals UMZ and INY.

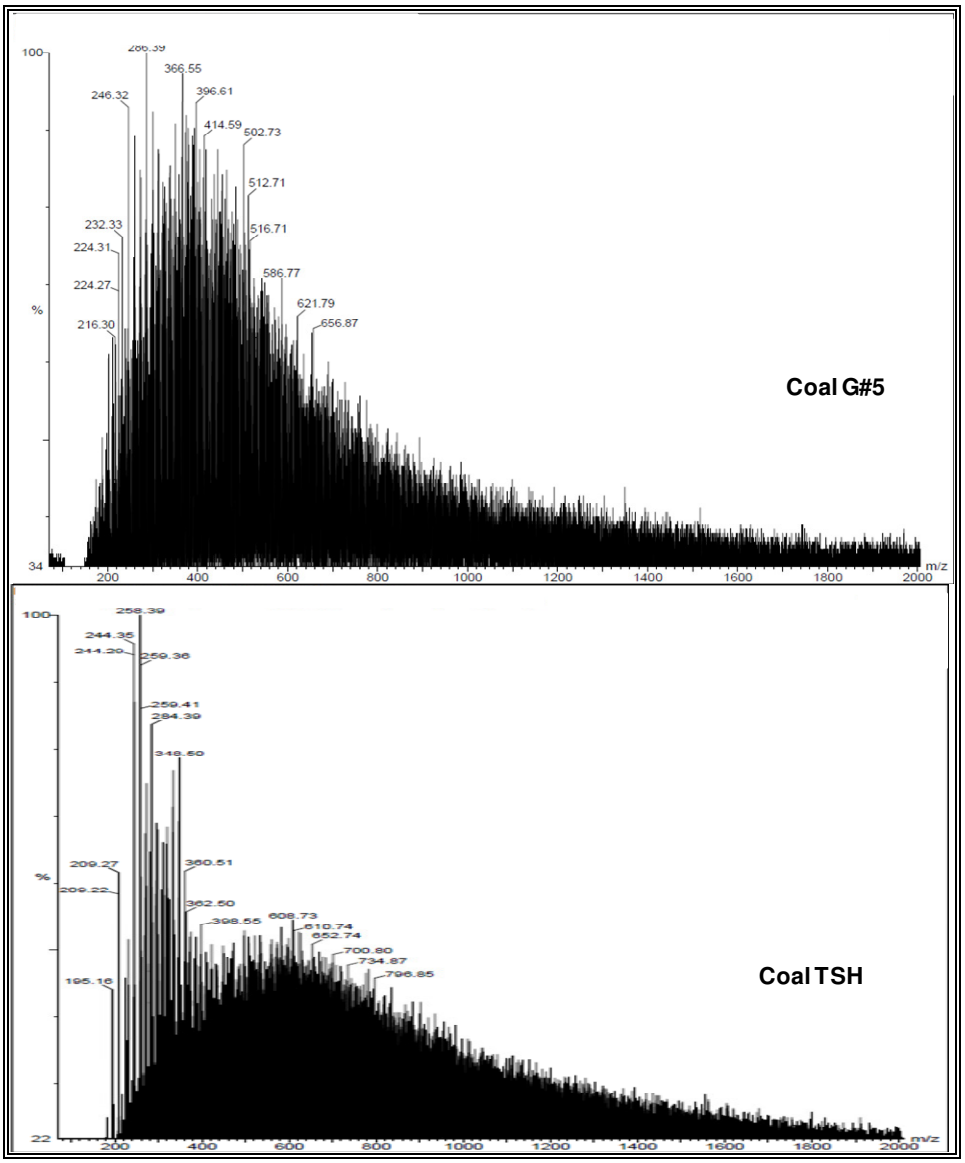

Figure 5.18 MALDI-TOF MS spectra of coals G#5 and TSH.

From the spectra it can be seen that all four coals showed molecular weight distributions ranging to approximately 1800 m/z. From a qualitative perspective it could be observed that the molecular weight distribution of coal TSH showed a slight shift to the higher molecular weights when compared to the other coals. The apex of the Lorentzian weight distributions were used to qualitatively compare the maximum molecular weight abundance of the four coals (Van Niekerk, 2008). By visual inspection it was found that the maximum molecular weight abundance of the four coals ranged between 397 m/z for coal G#5, 500 m/z for coal INY, 505 m/z for coal UMZ and 609 m/z for coal TSH. This indicates, although only from a qualitative viewpoint, that coal TSH contains predominately higher molecular entities, whilst coal G#5 contains relatively lower

molecular weight functionalities. The results for coals INY and UMZ are, however, quite comparable. The obtained results for the four coals are consistent with previous studies conducted on Argonne Premium coals (Herod *et al*., 1994; Miura *et al*., 2001) and two typical South African coals (Van Niekerk, 2008). From these studies it was concluded that coal exhibits an abundant molecular weight distribution in the molecular weight range smaller than a 1000 m/z. It should be noted that, although the LD-TOF technique is effective for establishing exact molecular mass distributions, it has the drawback of not being effective in quantitatively estimating the amounts of individual masses (Miura *et al*., 2001; Van Niekerk, 2008). Furthermore, the observed molecular weight distributions are only applicable to chemical functionalities within the coal samples with the ability to be volatized and to fly during the analyses. Non-volatile functionalities could therefore be underestimated.

5.4.1.5 High-resolution transmission electron microscopy (HRTEM) and image analyses

The HRTEM technique has been found, by numerous investigators, to be a valuable tool in the investigation of the distribution of aromatic layers within coals and coal-derived products (Mathews *et al*., 2010; Sharma *et al*., 2000; Sharma *et al*., 2001; Van Niekerk, 2008; Yang *et al*., 2006; Yoshizawa *et al*., 1998). A similar HRTEM acquisition methodology was followed as proposed by Sharma *et al*. (2000) and Van Niekerk (2008). The obtained micrographs displayed similar features to what was observed by Roberts (2012), Sharma *et al*. (2000) and Van Niekerk (2008). In some cases the micrograph quality was not as high in comparison to the micrographs published by Sharma *et al*. (2000). This can, however, be attributed to possible system drift that could have occurred during the analyses (Van Niekerk, 2008).

HRTEM images of each coal are shown in Figure 5.19. Visual inspection of multiple micrographs of the four coals shows that coal G#5 had a less oriented structure in comparison with the other three coals. In some cases more oriented layers could also be observed for coal TSH in comparison with coals INY and UMZ, although not evident in all the micrographs. These observations tend to be consistent with what was observed for the aromaticity and *DOI* values obtained from ^{13}C NMR and XRD analyses. It is therefore evident that coal G#5 contained fewer poly-condensed molecular units, with a less ordered structure.

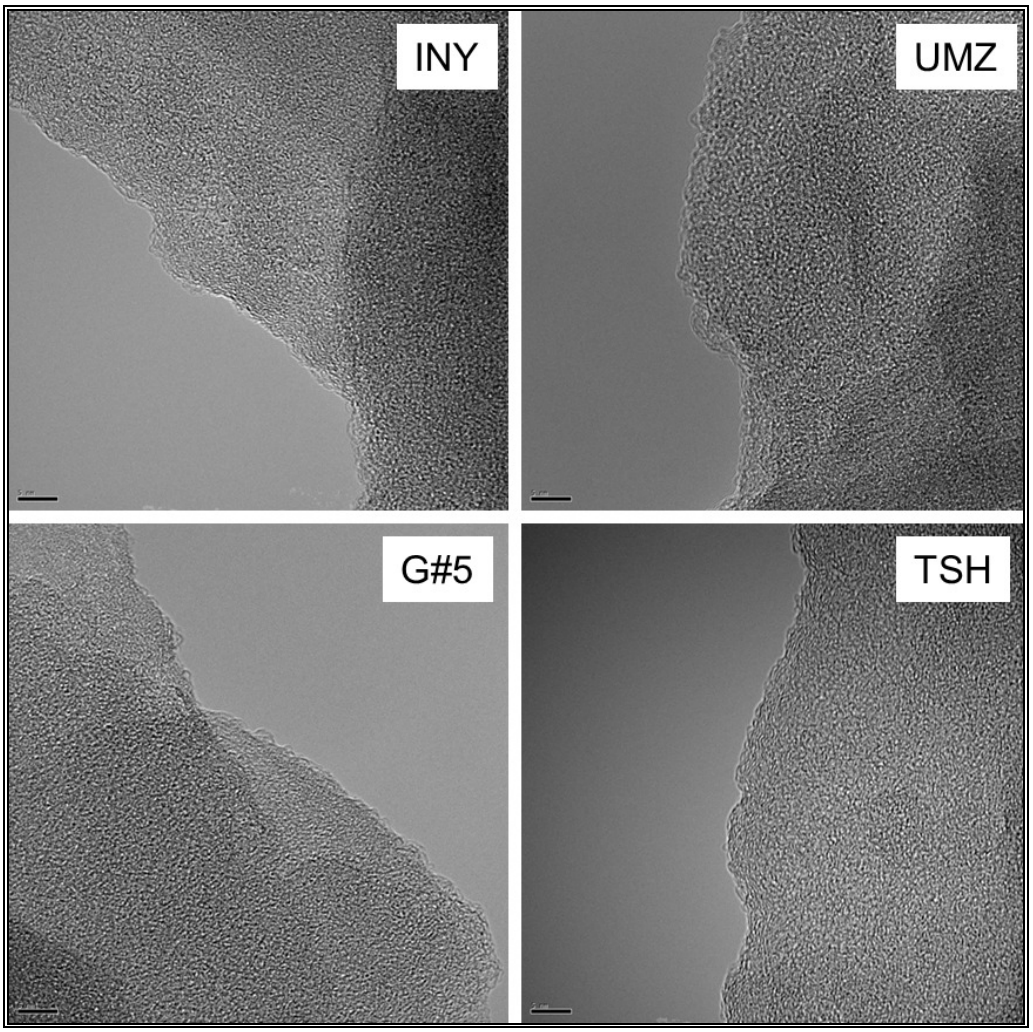

Figure 5.19 HRTEM micrographs for coals UMZ, INY, G#5 and TSH.

The more oriented structure of coal TSH differs from the observations made by Sharma *et al*. (2000) and Van Niekerk (2008) that inertinite-rich coals are more likely to contain oriented or aligned structures. This discrepancy can, however, be attributed to the higher rank and aromatic fraction of coal TSH.

The HRTEM micrographs of each coal were processed according to the method discussed in Section 5.3.1.4. An example of the obtained processed images from the cropping step to the binary conversion step, through to the final lattice-fringe extracted image is illustrated for coal TSH in Figure 5.20. From the Figure it is clear that the skeletonised image provides a good representation of the presence and orientation of the different fringes or aromatic rafts.

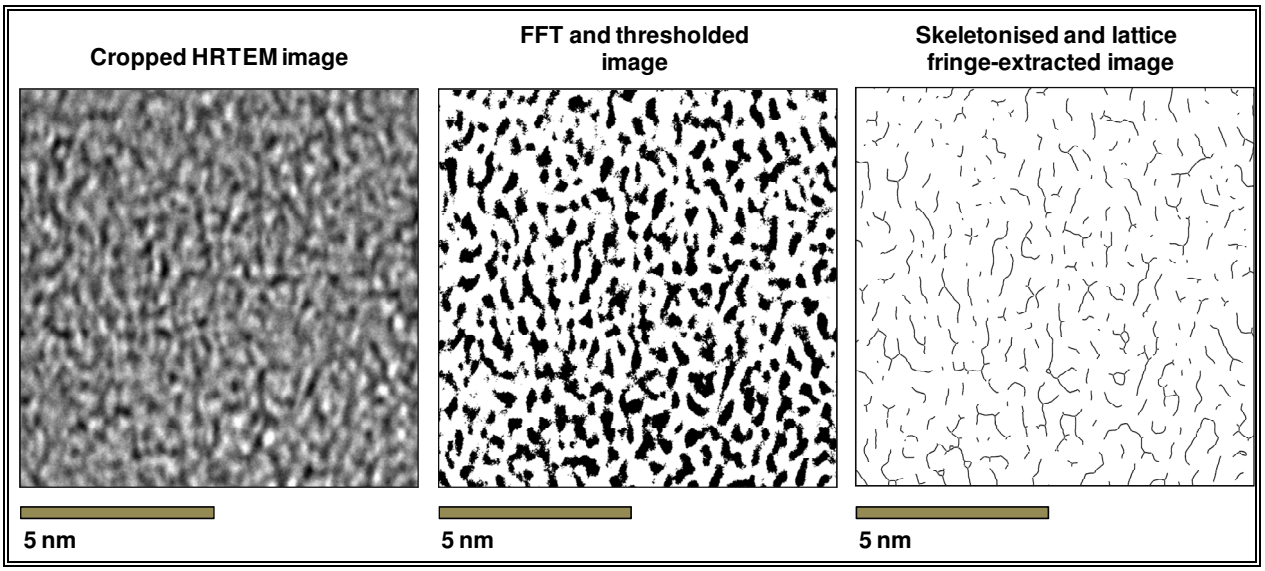

Figure 5.20 Overview of some of the processing steps during the lattice fringe-extraction of coal TSH.

The image processing toolkit of Reindeer Graphics was further applied to determine the length (in Angstroms) of each extracted aromatic fringe. A typical size-distribution (where the fringes are default coloured according to size) present in a fringe-extracted HRTEM image of coal TSH is illustrated in Figure 5.21.

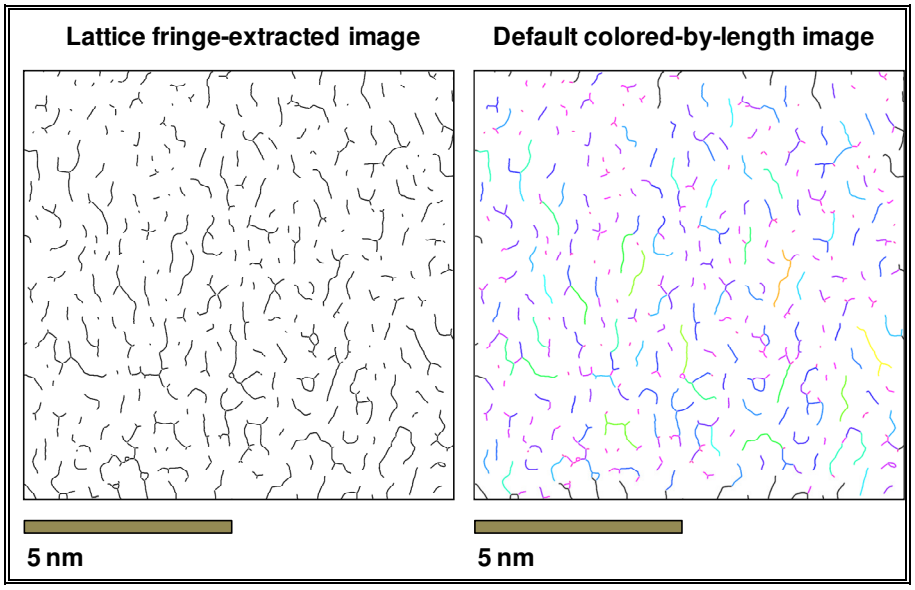

Figure 5.21 Coloured-by-length value distribution of coal TSH.

The lattice-fringe extracted image consists of small, intermediate and large aromatic features.

The segment selection tool of the image processing toolkit enables the selection of certain fringes in specified length ranges as illustrated for the small, intermediate and large size range of the lattice-fringe extracted HRTEM image of coal TSH (Figure 5.22). Similar results were obtained for coals UMZ, INY and G#5. Examples of the processed images of these three coals are provided in Appendix B.4 and B.5.

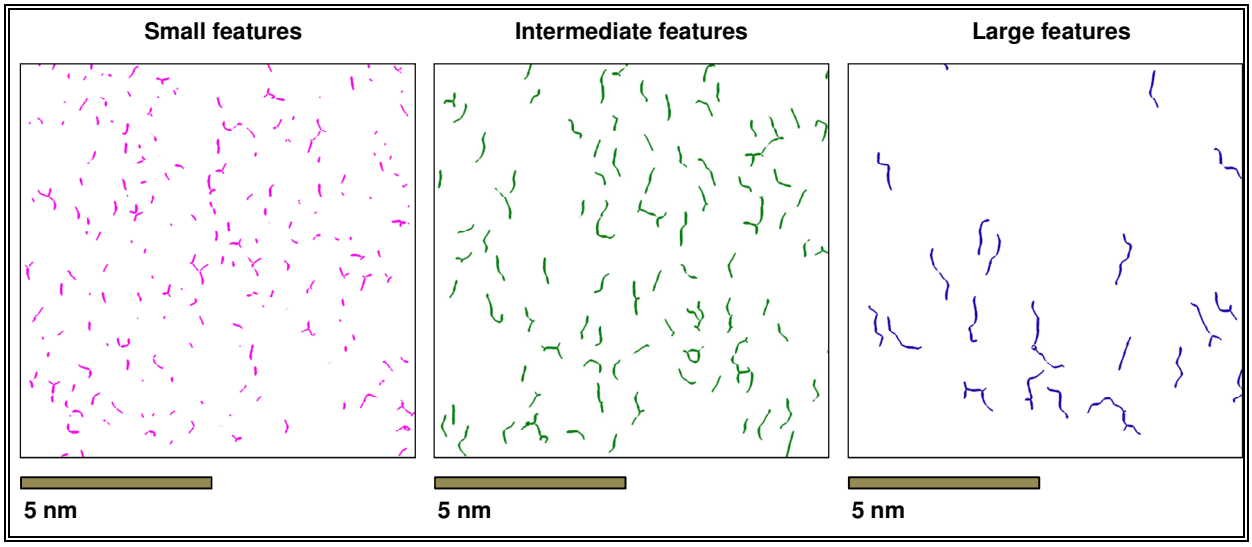

Figure 5.22 Selected fringes of coal TSH in different size-ranges.

Currently HRTEM is the only technique available for observing the molecular structure of coal (Sharma *et al*., 2000) and recent developments by Mathews *et al.* (2001) have enabled investigators to assign aromatic sizes to the extracted HRTEM images (Van Niekerk, 2008). In this method the aromatic fringes are represented by parallelogram sheets of different sizes (Mathews *et al*., 2001; Van Niekerk, 2008). Although not truly an indication of the large molecular moieties in coal, this approach provides a reasonable starting point for qualitatively describing the diversity and distribution of the aromatic rafts present in coal (Van Niekerk, 2008).

Other authors such as Solum *et al*. (1989, 2001) have, however, represented the aromatic rafts as either linear or circular catenations during lattice calculations. A typical 6x6 parallelogram-shape aromatic raft is presented in Figure 5.23. Each parallelogram-shaped raft consists of two characteristic lengths: *MaxL* and *MinL* (Van Niekerk, 2008).

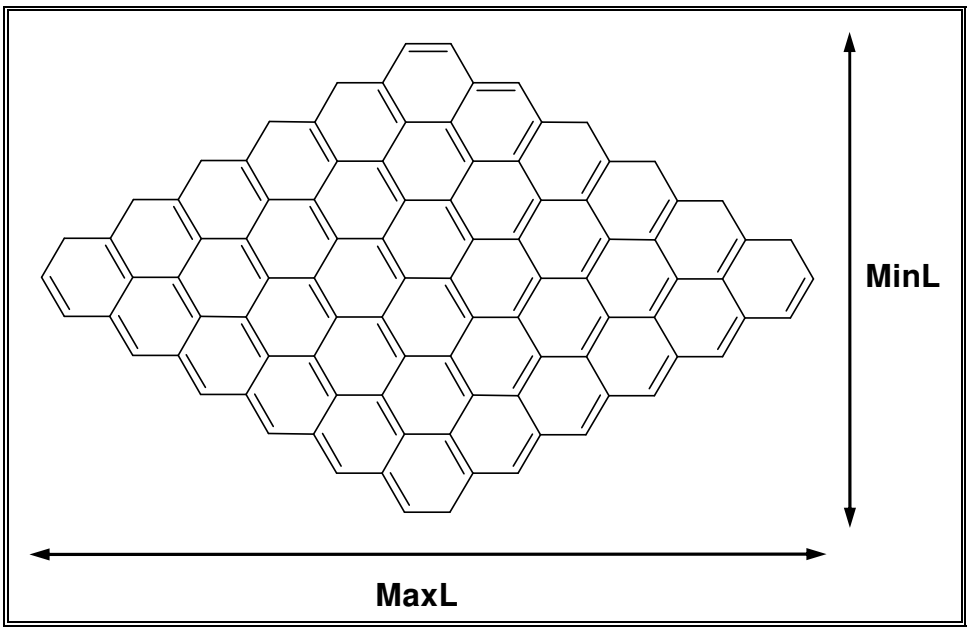

Figure 5.23 Example of a 6x6 fringe with maximum (MaxL) and minimum (MinL) length.

These two important characteristic lengths were estimated for the parallelogram fringes ranging in size from benzene to up to 20x20 with the help of Material Studio 5.0 software (Roberts, 2012). The problem of spatial orientation does, however, exist when comparing parallelogram representations to lattice-extracted fringes from HRTEM (Van Niekerk, 2008). In order to eradicate this, a mean value (calculated from the *MaxL* and *MinL* values) was used to assign an aromatic catenation to each fringe. The obtained lengths for each aromatic raft are summarized in Table 5.9. The grouping ranges were constructed according to the process described by Mathews *et al*. (2010).

As an example, all fringes exhibiting sizes between 4.4 Å and 5.9 Å were assigned to the anthracene/phenanthrene catenation, while fringes between 5.9 Å and 9.9 Å were assigned to the 2x2 parallelogram catenation etc. Fringes with lengths smaller than 3 Å were assigned to benzene although this could have included some noise that was not totally removed during the filtering process.

The obtained fringes were therefore classified within the different parallelogram catenation groups and the relative frequency of each specific parallelogram raft size was expressed as a percentage of the total amount of fringes. For each cropped micrograph of each coal more than 4000 fringes were extracted and subjected to image analyses and aromatic raft size determination.

Table 5.9 Assignment of parallelogram sizes to HRTEM fringes (Roberts, 2012).

Parallelogram raft size	*MinL (Å)*	*MaxL (Å)*	*Mean (Å)*	*Grouping (Å)*
Benzene	2.5	2.9	2.7	< 3
Naphthalene	2.9	5.1	4.0	3 - 4.4
Anthracene/Phenanthrene	2.9	7.3	5.1	4.4 – 5.9
2x2	4.9	7.1	6.0	5.9 - 9.9
3x3	7.4	11.3	9.3	10.0 - 14.9
4x4	9.8	15.5	12.7	15.0 - 19.9
5x5	12.3	19.8	16.0	20.0 - 24.9
6x6	14.7	24.0	19.4	25.0 - 29.9
7x7	17.2	28.3	22.7	30.0 - 34.9
8x8	19.6	32.5	26.1	35.0 - 39.9
9x9	22.1	36.8	29.4	40.0 - 44.9
10x10	24.5	41.0	32.8	45.0 - 49.9
11x11	27.0	45.2	36.1	50.0 - 54.9
12x12	29.4	49.5	39.5	55.0 - 59.9
13x13	31.9	53.7	42.8	60.0 - 64.9
14x14	34.3	58.0	46.2	65.0 - 69.9
15x15	36.8	62.2	49.5	70.0 - 74.9
16x16	39.2	66.5	52.8	75.0 - 79.9
17x17	41.7	70.7	56.2	80.0 - 84.9
18x18	44.1	74.9	59.5	85.0 - 89.9
19x19	46.6	79.1	62.8	90.0 - 94.9
20x20	49.0	83.3	66.2	95.0 - 99.9

The obtained aromatic raft size distributions with respect to fringe length for coals INY, UMZ, G#5 and TSH are shown respectively in Figures 5.24 and 5.25. The aromatic raft size distributions of all four coals exhibited similar Lorentzian type behaviour, which is consistent with what was observed for the MALDI-TOF results. All four coals exhibit a greater abundance of fringes concentrated in the 2x2, 3x3, 4x4 and 5x5 region, while the abundance of larger fringes decrease with increasing fringe length. Coals UMZ, INY and TSH are surprisingly similar in their distribution of aromatic fringes in the range extending from Benzene to 6x6. Coal TSH did,

however, show a slightly higher abundance of aromatic fringes in the range greater than 6x6, when compared to the other three coals.

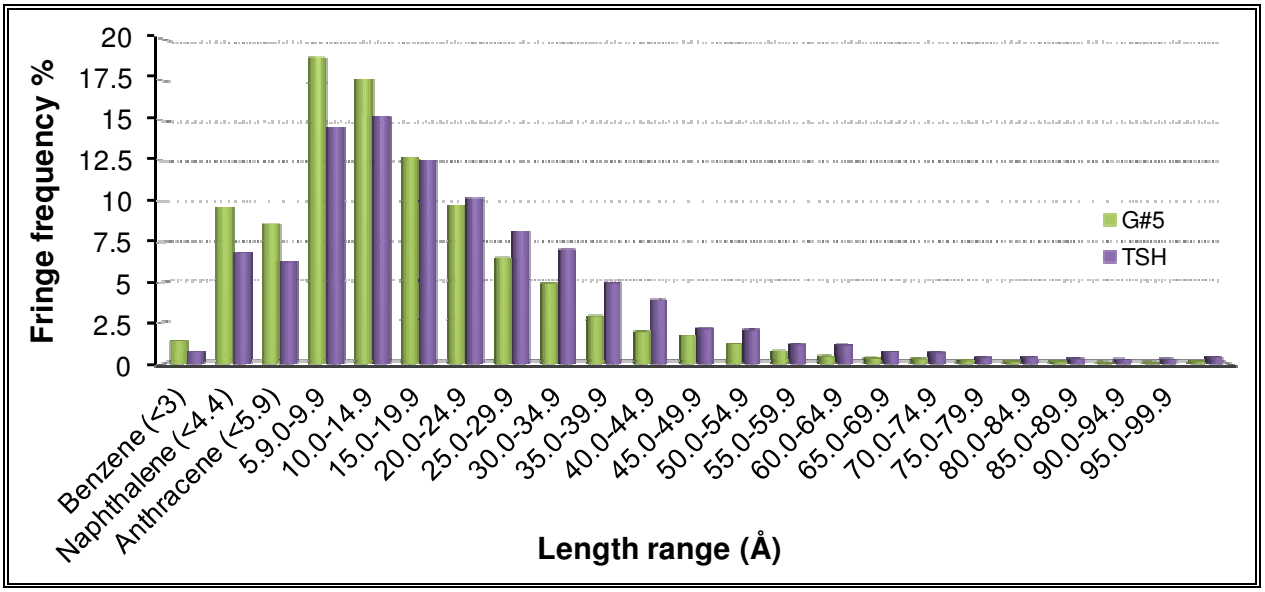

Figure 5.24 Aromatic raft size distribution w.r.t to fringe length for coals G#5 and TSH.

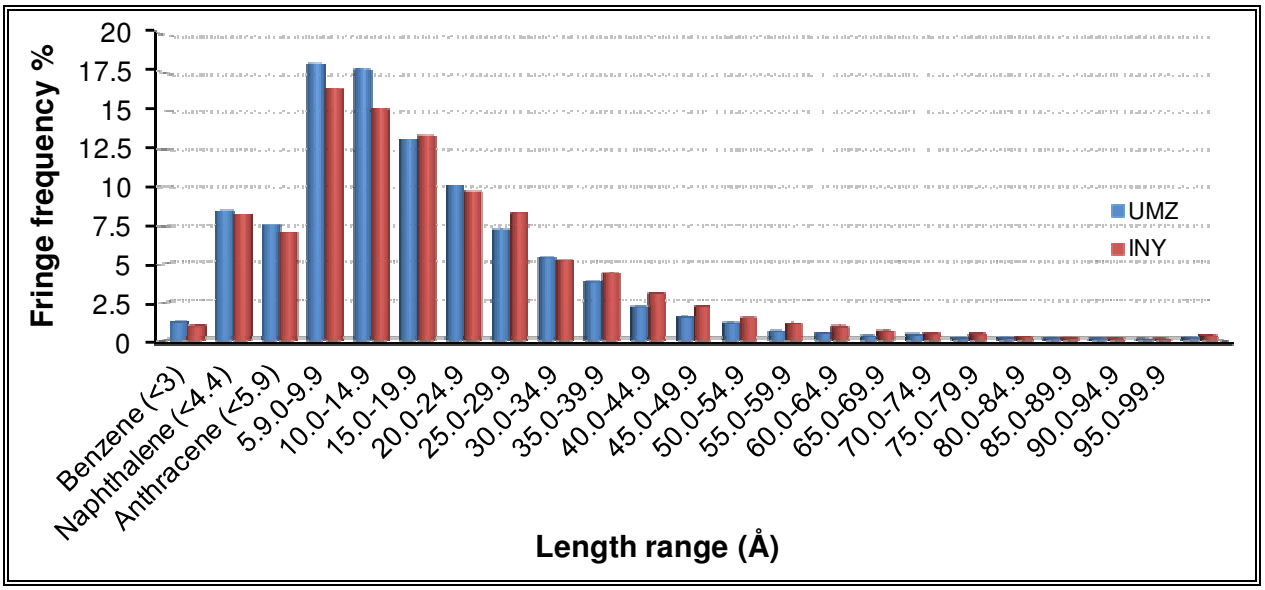

Figure 5.25 Aromatic raft size distribution w.r.t to fringe length for coals UMZ and INY.

In addition, in coal G#5, the aromatic rafts confined to the benzene to 3x3 fringe lengths were more abundant. The above-mentioned observations are consistent with what was determined through ^{13}C-NMR, that coal G#5 is the least aromatic while the inverse is true for coal TSH. This supporting data confirms the fact that coal G#5 is less aromatic and poly-condensed than the

other three coals. The method as proposed by Mathews *et al*. (2010) was used to relate the fringe lengths of parallelogram shaped aromatic fringes to the minimum (C_{min}) and maximum (C_{max}) number of carbon atoms that can be enclosed in the fringe. In addition, the average (C_{ave}) of these two values can be used to estimate the molecular weight of each individual fringe (Mathews *et al*., 2010; Van Niekerk, 2008). The explicit relations used to perform the above-mentioned estimations are provided in the following three equations:

$$C_{\min} = 0.4312 \times fringe\ \ length^{1.7132} \qquad \text{Equation (5.17)}$$

$$C_{\max} = 0.7981 \times fringe\ \ length^{1.7964} \qquad \text{Equation (5.18)}$$

$$Mw = \left(12.106 \times C_{ave}\right) + \left(\left(0.1806 \times C_{ave}\right) + 8.98\right) \qquad \text{Equation (5.19)}$$

The molecular weight distributions obtained from this method is illustrated graphically for all four coals in Figure 5.26 and 5.27.

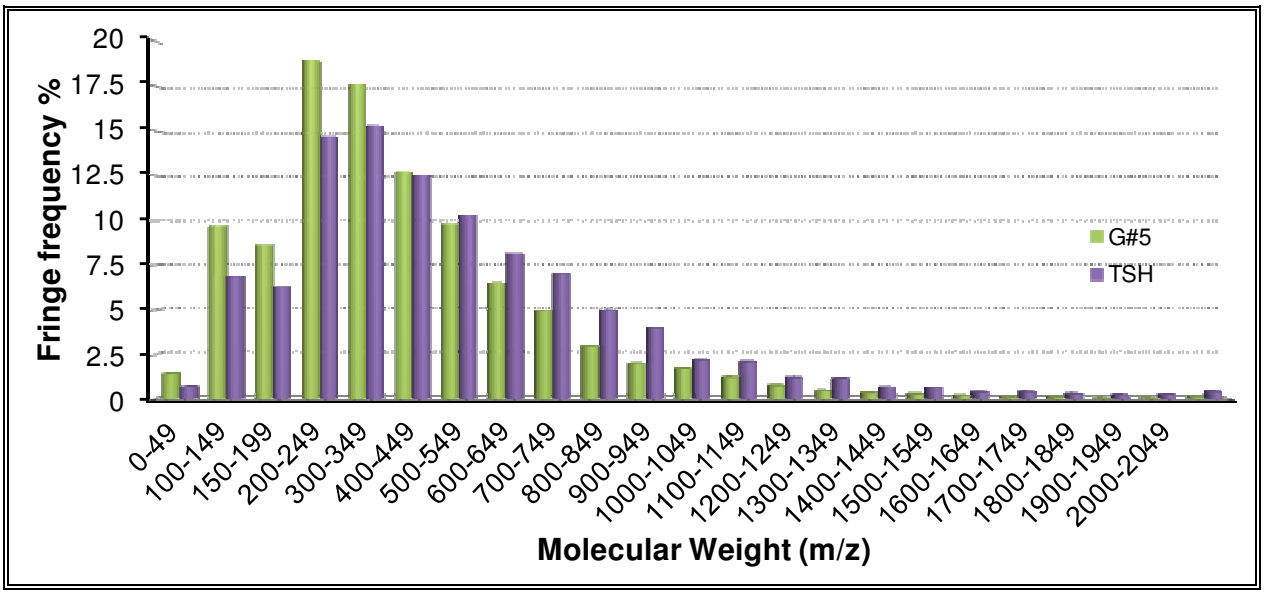

Figure 5.26 Molecular weight distribution from HRTEM for coals G#5 and TSH.

Similar observations were made as in the case of the fringe length distributions described in Figures 5.24 and 5.25. A comparison with the MALDI-TOF results reveals that a very good similarity exists between the mass distributions obtained from HRTEM and from MALDI-TOF. The obtained molecular weight distributions from HRTEM displayed the same Lorentzian type behaviour to what was observed from MALDI-TOF.

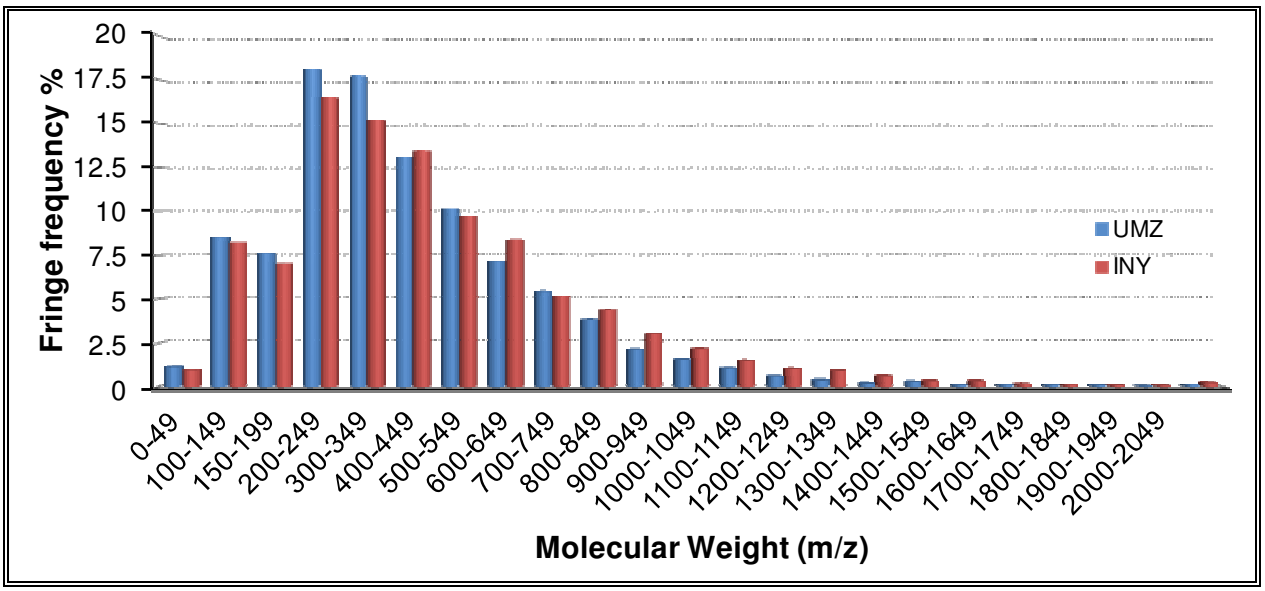

Figure 5.27 Molecular weight distribution from HRTEM for coals UMZ and INY.

Although, if only from a qualitative point of view, a good similarity exists between the molecular weight distributions obtained from the two methods, it should be noted that the results obtained from MALDI-TOF includes both aromatic and aliphatic molecular fragments, whereas HRTEM image analyses only accounts for the aromatic fringes. Table 5.10 provides a comparison between the average molecular weight as obtained from ^{13}C NMR, MALDI-TOF MS and HRTEM, respectively.

Table 5.10 Comparison between average molecular weight from different analytical methods.

Analytical method	*INY*	*UMZ*	*G#5*	*TSH*
Molecular weight from ^{13}C NMR	419 m/z	348 m/z	448 m/z	400 m/z
Molecular weight from MALDI-TOF MS	500 m/z	480 m/z	397 m/z	609 m/z
Molecular weight from HRTEM	467 m/z	427 m/z	412 m/z	506 m/z

It should be noted that the average molecular weight obtained from ^{13}C NMR is for an average molecular cluster, while the average molecular weight from MALDI-TOF MS is assigned to the apex of the molecular mass distribution of each coal. The average molecular weight from HRTEM was estimated from the relative frequencies of the different fringes. Good agreement was obtained between the three different analyses and the determined values were in reasonable order for each coal. The molecular weight values obtained from ^{13}C NMR and

MALDI-TOF MS therefore supports the current use of the HRTEM technique for characterizing aromatic fringes. This in agreement with what was observed by Van Niekerk (2008).

5.5 Summary

The advanced characterization analyses conducted on the samples revealed the respective molecular and structural nature of each coal. Some of the important characteristic properties obtained for the four coals are summarised in Table 5.11.

Table 5.11 Summary of advanced characterisation results.

Property	*INY*	*UMZ*	*G#5*	*TSH*
Structural analyses				
Fraction Aromatics	0.74	0.77	0.66	0.81
Fraction aliphatics	0.26	0.23	0.34	0.19
Number of bridges and loops per cluster	4.4	3.9	2.8	0.2
Number of side chains per cluster	1.1	0.7	1.7	2.1
Total molecular weight per cluster (g/mol)	419.2	348.0	448.2	400.4
Amorphous fraction of carbon	0.58	0.59	0.67	0.52
Degree of disorder index (*DOI*)	0.69	0.69	0.78	0.61
Highest aromatic fringe distribution	2x2	2x2	2x2	3x3
Average molecular weight (g/mol)	467.1	426.8	411.7	506.0

Coal aromaticity (as determined by ^{13}C NMR) was found to increase in the order of G#5 < INY < UMZ < TSH, and showed good agreement with the random vitrinite reflectance (rank) determined for each coal. The NMR derived lattice parameters indicated that coal TSH had a slightly larger cluster size than the other three coals (24 carbons for coal TSH and 19-21 carbons for the other three coals). The Witbank coals contained more attachments (5-6 per cluster) confined to bridge and/or loop structures, whilst coal TSH only contained 3 attachments per cluster predominantly characterised as side chain functionalities. XRD carbon crystallite analyses provided additional evidence of the highly poly-condensed aromatic nature of each coal. Structural parameters such as the amorphous fraction of carbon and degree of disorder index (*DOI*) were determined directly from the corrected diffractograms of each coal and were found to be the highest for coal G#5 (0.67 and 0.78 respectively), while the lowest values were

estimated for coal TSH (0.52 and 0.61, respectively). MALDI-TOF MS analyses showed that all four coals had similar molecular weight distributions ranging up to approximately 1800 m/z, with average molecular weights ranging between 300-500 m/z. Coal TSH was characterised with a maximum abundance at a higher molecular mass of 609 m/z in comparison to the other coals. HRTEM analyses showed a similar Lorentzian-type behaviour as observed for the MALDI-TOF MS results. From the HRTEM analyses it was evident that coal TSH contained larger amounts of aromatic fringes (average size range of 3x3) confined to higher molecular masses. Good agreement was found between average molecular masses determined from ^{13}C NMR, MALDI-TOF MS and HRTEM, respectively.

Bibliography

Assumption, H. 2010. Characterization of coal samples. NMR results report. University of Stellenbosch. RSA. 28 p.

Botto R.E., Wilson, R. & Winans, R.E. 1987. Evaluation of the reliability of solid ^{13}C NMR spectroscopy for the quantitative analysis of coals: Study of whole coals and maceral concentrates. *Energy & Fuels*, 1:173-181.

Choi, C.Y., Muntean, J.V., Thompson, R.A., & Botto, R.E. 1989. Characterization of coal macerals using combined chemical and NMR spectroscopic methods. *Energy & Fuels*, 3:528–533.

Ergun, S & Tiensuu, V. H. 1959. Interpretation of the intensities of X-rays scattered by coals. *Fuel*, 38: 64-78.

Feng, B., Bhatia, S.K. & Barry, J.C. 2003. Variation of the crystalline structure of coal char during gasification. *Energy & Fuels,* 17(3): 744-754.

Franklin, R.E. 1951. The structure of graphitic carbons. *Acta Crystallographica*, 4: 253-261.

Franz, J.A., Garcia, R., Linehan, J.C., Love, G.D. & Snape, C.E. 1992. Single-pulse excitation ^{13}C NMR measurements on the Argonne Premium coal samples. *Energy & Fuels*, 6: 598-602.

Gupta, R. 2007. Advanced Coal Characterisation: A Review. *Energy & Fuels*, 21: 451-460.

Herod, A.A., LI, C.Z., Parker, J.E., John, P, Johnson, C.A.F., Smith, G.P., Humphrey, P., Chapman, J.R. & Kandiyoti, R. 1994. Characterisation of coal by matrix-assisted laser-desorption ionization mass-spectrometry. 1. The Argonne coal samples. *Rapid Communications in Mass Spectrometry*, 8(10): 808-814.

Iwashita, N. & Inagaki, M. 1993. Relations between structural parameters obtained by X-ray powder diffraction of various carbon materials. *Carbon*, 31(7):1107-1113.

Lu, L., Sahajwalla, V., Kong, C. & Harris, D. 2001. Quantitative X-ray diffraction analysis and its application to various coals. *Carbon*, 39:1821-1833.

Lu, L., Kong, C., Sahajwalla, V. & Harris, D. 2002. Char structural ordering during pyrolysis and combustion and its influence on char reactivity. *Fuel*, 81: 1215-1225.

Maity, S. & Mukherjee, P. 2006. X-ray structural parameters of some Indian coals. *Current Science,* 91(3): 337-340.

Mathews, J.P., Jones, A.D., Pappano, P.J., Hurt, R. & Schobert, H.H. 2001. New insights into coal structure from the combination of HRTEM and laser desorption ionization mass spectrometry. (*In* Proceedings of the 11th International Conference on Coal Science held in San Francisco, CA, 2001. San Francisco, CA.)

Mathews, J.P., Fernandez-Also, V., Jones, A.D. & Schobert, H.H. 2010. Determining the molecular weight distribution of Pocahontas No.3 low-volatile bituminous coal utilizing HRTEM and laser desorption ionization mass spectra data. *Fuel,* 89: 1461-1469.

Miknis, F.P., Turner, T.F., Ennen, L.W. & Netzel, D.A. 1988. NMR characterisation of coal pyrolysis products. *Fuel*, 67:1568-1577.

Miura, K., Shimada, M., Mae, K. & Sock, H.Y. 2001. Extraction of coal below 350℃ in flowing non-polar solvent. *Fuel*, 80(11): 1573-1582.

Muntean, J.V., Stock, L.M. & Botto, R.E. 1988. Improving the reliability of quantitative solid-state ^{13}C NMR analysis of coal. *Energy & Fuels*, (2): 108-110.

Muntean, J.V. & Stock, L. M. 1991. Bloch decay solid-state ^{13}C NMR spectroscopy of the samarium iodide treated Argonne premium coals. *Energy & Fuels*, (5): 765-767.

Okolo, G. 2010. The effects of chemical and physical properties of chars derived from inertinite-rich, high ash coals on gasification reaction kinetics. University of North-West: Potchefstroom. RSA. (Dissertation-M.Eng). 275p.

Orent, A.M., Solum, M.S., Sethi, N.K., Pugmire, R.J. & Grant, D. M. 1992. Advances in Coal Spectroscopy. New York: Plenum Press.

Oya, A., Mochizuki, M., Otani, S. & Tomizuka, I. 1979. An electron microscopic study on the turbostratic formed in phenolic resin carbon by catalytic action of finely dispersed nickel. *Carbon,* 17: 71-76.

Perry, S.T., Hambly, E.M., Fletcher, T.H., Solum, M.S. & Pugmire, R.J. 2000. Solid state ^{13}C NMR characterisation of matched tars and chars from rapid coal devolatilization. (*In* Proceedings of the Combustion Institute. Volume 28. p. 2313-2319).

Roberts, M. 2012. The molecular structure of selected South African coal-chars to elucidate fundamental principles of coal gasification. Potchefstroom: University of North-West. RSA. (Thesis-Ph.D). (Unpublished).

Sharma, A., Kyotani, T. & Tomita, A. 1999. A new quantitative approach for microstructural analysis of coal char using HRTEM images. *Fuel*, 78: 1203-1212.

Sharma, A., Kyotani, T. & Tomoita, A. 2000. Comparison of structural parameters of PF carbon from XRD and HRTEM techniques. *Carbon,* 38(14): 1977-1984.

Sharma, A., Kyotani, T. & Tomoita, A. 2001. Quantitative evaluation of structural transformations in raw coals on heat-treatment using HRTEM technique. *Fuel,* 80: 1467-1473.

Shiraishi, M. & Kobayashi, K. 1973. An X-ray study of coal tar pitch. *Bulletin of the Chemical Society of Japan,* 46: 2575-2578.

Smith, K.L., Smoot, L.D., Fletcher, T.H. & Pugmire, R.J. 1994. The structure and reaction processes of coal. New York: Plenum Press. 473p.

Solum, M.S., Pugmire, R.J. & Grant, D.M. 1989. ^{13}C Solid-State NMR of Argonne Premium Coals. *Energy & Fuels*, 3:187-193.

Solum, M.S., Sarofim, A.F., Pugmire, R.J., Fletcher, T.H. & Zhang, H. 2001. ^{13}C NMR Analysis of Soot Produced from Model Compounds and Coal. *Energy & Fuels,* 15:961-971.

Strydom, C.A., Bunt, J.R., Schobert, H.H. & Raghoo, M. 2011. Changes to the organic functional groups of an inertinite rich medium rank bituminous coal during acid treatment process. *Fuel Processing Technology*, 92: 764-770.

Suggate, R.P. & Dickinson, W.W. 2004. Carbon NMR of coals: the effects of coal type and rank. *International Journal of Coal Geology*, 57:1-22.

Takagi, H., Maruyama, K., Yoshizawa, N., Yamada, Y.& Sato, Y. 2004. XRD analysis of carbon stacking structure in coal during heat treatment. *Fuel*, 83: 2427-2433.

Trejo, F., Ancheyta, J., Morgan, T.J., Herod, A.A. & Kandiyoti, R. 2007. Characterization of asphaltenes from hydrotreated products by SEC, LDMS, MALDI, NMR, and XRD. *Energy & Fuels*, 21: 2121-2128.

Van der Merwe, G.L. 2010. The influence of particle size and devolatilization conditions on the CO_2 gasification of Highveld coal. Potchefstroom: University of North-West. RSA. (Dissertation-M.Eng). 131p.

Van Niekerk, D. 2008. Structural elucidation, molecular representation and solvent interactions of vitrinite-rich and inertinite-rich South African coals. Pennsylvania: Pennsylvania State University. USA. (Thesis-PhD). 195p.

Van Niekerk, D., Pugmire, R.J., Solum, M.S., Painter, P.C. & Mathews, J.P. 2008. Structural characterisation of vitrinite-rich and inertinite-rich Permian-aged South African bituminous coals. *International Journal of Coal Geology*, 76: 290-300.

Wang, J., Morishita, K. & Takarada, T. 2001. High-temperature interactions between coal char and mixtures of calcium oxide, quartz and kaolinite. *Energy & Fuels,* 15: 1145-1152.

Watt, M., Fletcher, T.H., Bai, S., Solum, M.S. & Pugmire, R.J. 1996. Chemical structure of coal tar during devolatilization. *Proceedings of the Combustion Institute*, 26(2): 3153-3160).

Wu, S., Gu, J., Zhang, X., Wu, Y.& Gao, J. 2008. Variation of carbon crystalline structures and CO_2 gasification reactivity of Shenfu coal chars at elevated temperatures. *Energy & Fuels*, 22:199-206.

Yang, J., Cheng, S., Wang, X., Zhang, Z, Liu, X. & Tang, G. 2006. Quantitative analysis of microstructure of carbon materials by HRTEM. *Transactions of Nonferrous Metals Society of China,* 16: 796-803.

Yoshizawa, N., Yamada, Y. & Shiraishi, M. 1998. TEM lattice images and their evaluation by image analysis for activated carbons with disordered microtexture. *Journal of Materials Science*, 33: 199-206.